chapter
17

Single Photon Emission Computed Tomography

As discussed in Chapter 16, a rotating gamma camera can be used to acquire data for computed tomographic (CT) images. This approach to tomography, which is employed with radionuclides that emit single γ rays or multiple γ rays with no angular correlations, is known as *single photon emission computed tomography* (*SPECT*). In this chapter, we describe the design features and performance characteristics of SPECT systems. We also discuss some practical aspects of SPECT imaging and some of its major clinical applications. A second form of tomographic nuclear medicine imaging, *positron emission tomography* (*PET*), uses radionuclides that decay by positron emission. PET imaging systems and their characteristics are discussed in Chapter 18. Multimodality systems that combine SPECT or PET with x-ray CT are discussed in Chapter 19.

A. SPECT SYSTEMS

1. Gamma Camera SPECT Systems

Almost all commercially available SPECT systems are based on the gamma camera detector that was described in detail in Chapters 13 and 14. A single gamma camera head, mounted on a rotating gantry, is sufficient to acquire the data needed for tomographic images. The gamma camera acquires two-dimensional (2-D) projection images at equally spaced angular intervals around the patient. These images provide the 1-D projection data needed for reconstructing cross-sectional images using the techniques described in Chapter 16. Typically, clinical SPECT images

are reconstructed on a matrix of 64×64 or 128×128 pixels. Cross-sectional images are produced for all axial locations (slices) covered by the field of view (FOV) of the gamma camera, resulting in a stack of contiguous 2-D images that form a 3-D image volume.

The number of angular projections (or views) needed when using a standard parallel-hole collimator can be calculated using Equation 16-15. Because the resolution of a general-purpose parallel-hole collimator is approximately 1 cm at a distance of 10 cm from the collimator (see Fig. 14-16), the number of views required generally is between 64 and 128, for a FOV ranging from 20 to 60 cm in diameter. Although data acquired over an arc of 180 degrees are sufficient for tomographic reconstruction in SPECT, there are advantages in terms of resolution uniformity and correction for γ-ray attenuation in acquiring data over a full 360-degree arc. This is discussed in Section B.1.

The sensitivity of a SPECT system can be improved by incorporating multiple detector heads in the system. Both dual-headed and triple-headed SPECT systems are available, with dual-headed systems being the most commonly encountered. These systems allow two or three angular projections to be acquired simultaneously. For the same total data acquisition time, each projection can be recorded two or three times, leading to a twofold or threefold increase in the total number of counts acquired for the image. Alternatively, a multihead system can be used to acquire the same number of counts in one half or one third the time needed with a single-head system. This can be useful for dynamic SPECT imaging to observe changes

in the distribution of a radiopharmaceutical as a function of time (Section D). One also could replace the parallel-hole collimator with a converging collimator to obtain improved sensitivity (see Fig. 14-21); however, this results in a smaller FOV (see Fig. 13-7).

Photographs of single-headed and dual-headed gamma cameras that are capable of SPECT imaging are shown in Figures 13-11 and 13-12. In dual-headed SPECT systems, the detector heads are typically placed at 180 degrees relative to each other for whole-body SPECT imaging, and at 90 degrees relative to each other for cardiac imaging. In some systems the location of the detector heads is fixed, whereas in others, they can be adjusted by the operator. Figure 13-12 shows a system in which the detector head orientations can be changed. In addition to mechanical capabilities for rotating the detector heads, gamma camera systems intended for SPECT imaging must be provided with computer capabilities and software for image reconstruction, for attenuation and scatter corrections, and for display and analysis of 3-D image volumes. The ability to perform conventional planar imaging as well as tomographic imaging is a very useful feature of these cameras.

Many SPECT systems have more sophisticated gantries that allow the detector heads to trace out elliptical rather than circular orbits. Some even allow orbits that follow the contours of the patient. The body contour can be determined by an initial scout scan that, for example, uses an infrared light source and camera to trace the outline of the patient and the bed as a function of angle. The importance of this feature is evident from Figure 14-16, which shows the rapid degradation in spatial resolution with increasing distance of the object from the collimator. As shown in Figure 17-1, elliptical orbits or orbits that follow the contours of the patient allow the detector to pass closer to the patient than would be the case with circular orbits, which can lead to significant improvements in spatial resolution.

2. SPECT Systems for Brain Imaging

A disadvantage common to all of the SPECT systems described in the preceding section is that the detector heads must be rotated around the patient to record the multiple projections required for tomographic reconstruction. Because of the mechanical motions involved and the bulk of the detector head or heads, the shortest time in which a complete set of projections can be recorded generally is
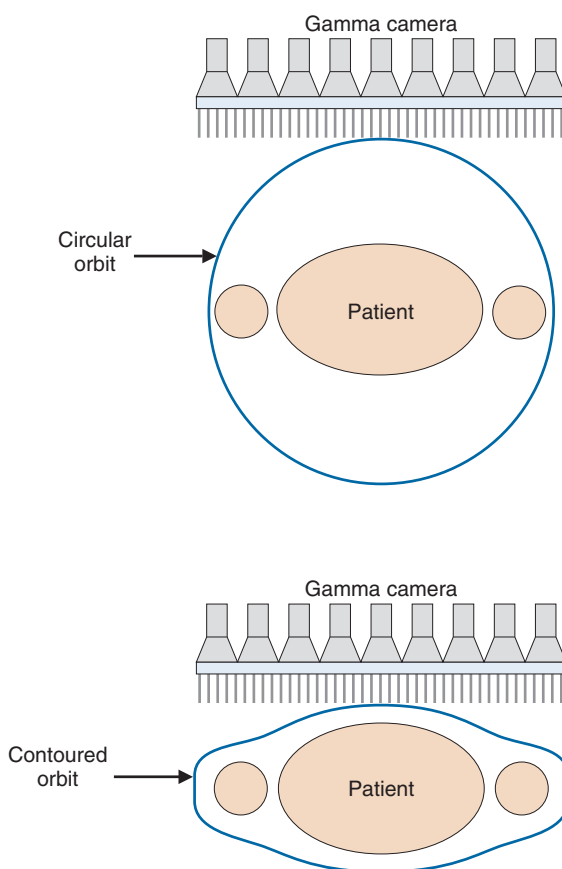

FIGURE 17-1 Illustration of circular (*top*) and contoured (*bottom*) orbits for SPECT imaging. The contoured orbit minimizes the distance of the detector from the patient, thus optimizing spatial resolution.

several minutes. For imaging fast biologic processes, it would be desirable to acquire a full set of projections in a few seconds. Furthermore, traditional collimator design limits reconstructed spatial resolution to 1 cm or greater, which is inadequate for some applications in the human brain. A number of efforts have been made toward addressing these limitations. Although they involve specialized systems that are not currently commercially available, we describe briefly some of the concepts involved to illustrate possible alternatives to performing SPECT with a rotating gamma camera.

The University of Michigan *SPRINT II* system[1] employs 11 γ-ray detectors in a polygonal arrangement, each detector consisting of 44 thin bars of sodium iodide [NaI(Tl)] scintillator (dimensions 3-mm-wide × 13-mm-deep × 15-cm-long) coupled to an array of twenty 38-mm-diameter photomultiplier (PM) tubes arranged behind the NaI(Tl) bars in a close-packed hexagonal array. In-slice

collimation is achieved using a lead aperture ring, with 12 equally spaced 2.4-mm-wide slits, that rotates in front of the stationary detector array (Fig. 17-2A). Axial collimation is achieved using a set of stacked stationary lead foils. As the collimator ring rotates through one slit interval (30 degrees), the system acquires a complete set of fan-beam projection data.

A system based on similar principles is the *CERASPECT* system.[2] In this case, the detector is a single annular NaI(Tl) crystal (31 cm inner diameter × 8 mm thick × 13 cm wide) coupled to 63 5-cm diameter PM tubes via glass light guides (Fig. 17-2B). A parallel-hole collimator with six segments rotates in front of the detector, simultaneously providing six angular views. Each collimator segment has a different FOV. This gives a higher weighting to activity at the center of the object (which is viewed by all six collimator segments) in comparison to activity toward the periphery of the object (which is seen by a smaller number of collimator segments). This nonuniform weighting helps compensate for the effects of photon attenuation (see Sections B.1 and B.2) and provides more uniform signal-to-noise ratio across the image.

Both of these systems were designed primarily for brain imaging applications, and both provide better image resolution than a conventional SPECT system by placing the collimated detector relatively close to the head. The reconstructed spatial resolution is approximately 8 mm at the center of the brain, improving to approximately 5 mm at the edge of the brain. By comparison, a typical single-head SPECT system operated with a radius of rotation of 12.5 cm (appropriate for brain imaging) would have a resolution of approximately 12.5 mm full width at half maximum (FWHM) at the center of the brain (see Fig. 14-16). These systems also have roughly twofold to threefold higher sensitivity than a single-headed gamma camera with a general-purpose parallel-hole collimator, because multiple sets of projection data can be acquired simultaneously. This enables higher resolution to be achieved without injecting more radioactivity or lengthening the imaging time.

3. SPECT Systems for Cardiac Imaging

One of the most common uses for SPECT is to image myocardial function in patients with a range of cardiovascular diseases. Because of the relatively small FOV required for this application, and the increasing use of cardiac

SPECT in smaller clinics, dedicated and compact cardiac SPECT systems with high sensitivity have been developed. In contrast to the SPECT systems discussed so far, the majority of these cardiac systems involve the patient sitting upright in a chair during the examination.

Figure 17-3A shows a triple-headed SPECT system designed for cardiac applications.[3] Note the much smaller size of the detector heads compared with general-purpose SPECT systems. The detector heads use pixelated cesium iodide [CsI(Tl)] scintillator crystals, read out by avalanche photodiodes (Chapter 7, Section C.3). The size of each CsI(Tl) pixel is 6 mm, and there are 768 pixels in each detector head, providing a detector FOV of approximately 16 cm × 20 cm. In this system the detectors are fixed and the patient chair rotates to provide the necessary angular sampling for tomographic reconstruction. The distance between the detectors and the chair can be adjusted to accommodate patients of different size. With a low-energy, high-resolution (LEHR) collimator (see Table 14-1), the reported spatial resolution of the SPECT images is 11 mm (for a 20-cm detector-object separation) and the sensitivity for each detector head is ~72 cps/MBq (160 cpm/μCi). Because of the vertical orientation of the patient, the entire system can fit in a room as small as 2.4 m × 2.4 m.

Another type of cardiac SPECT system replaces standard scintillation Anger camera designs with detector heads made up of pixels of the dense semiconductor cadmium zinc telluride (CZT) (Chapter 7, Section B).[4] This system contains 10 small detector heads, distributed in an arc over the chest of the patient (Fig. 17-3B). Each detector head [2-mm CZT pixels tiled on a 40-mm (transaxial) by 160-mm (axial) area] is equipped with a parallel-hole collimator and can rotate independently to sample different projection angles, enabling a complete projection dataset to be acquired for tomographic reconstruction. The patient chair is stationary. The reconstructed spatial resolution is quite dependent on the location in the FOV, and is nonisotropic, ranging between approximately 8 and 14 mm. The sensitivity of the system is on the order of ~400 cps/MBq (900 cpm/μCi) for each detector head. The high sensitivity derives from the use of a shorter collimator with larger holes compared with the LEHR collimator.

A third design employs principles similar to the brain system shown in Figure 17-2A and described in Section 2. A multislit collimator
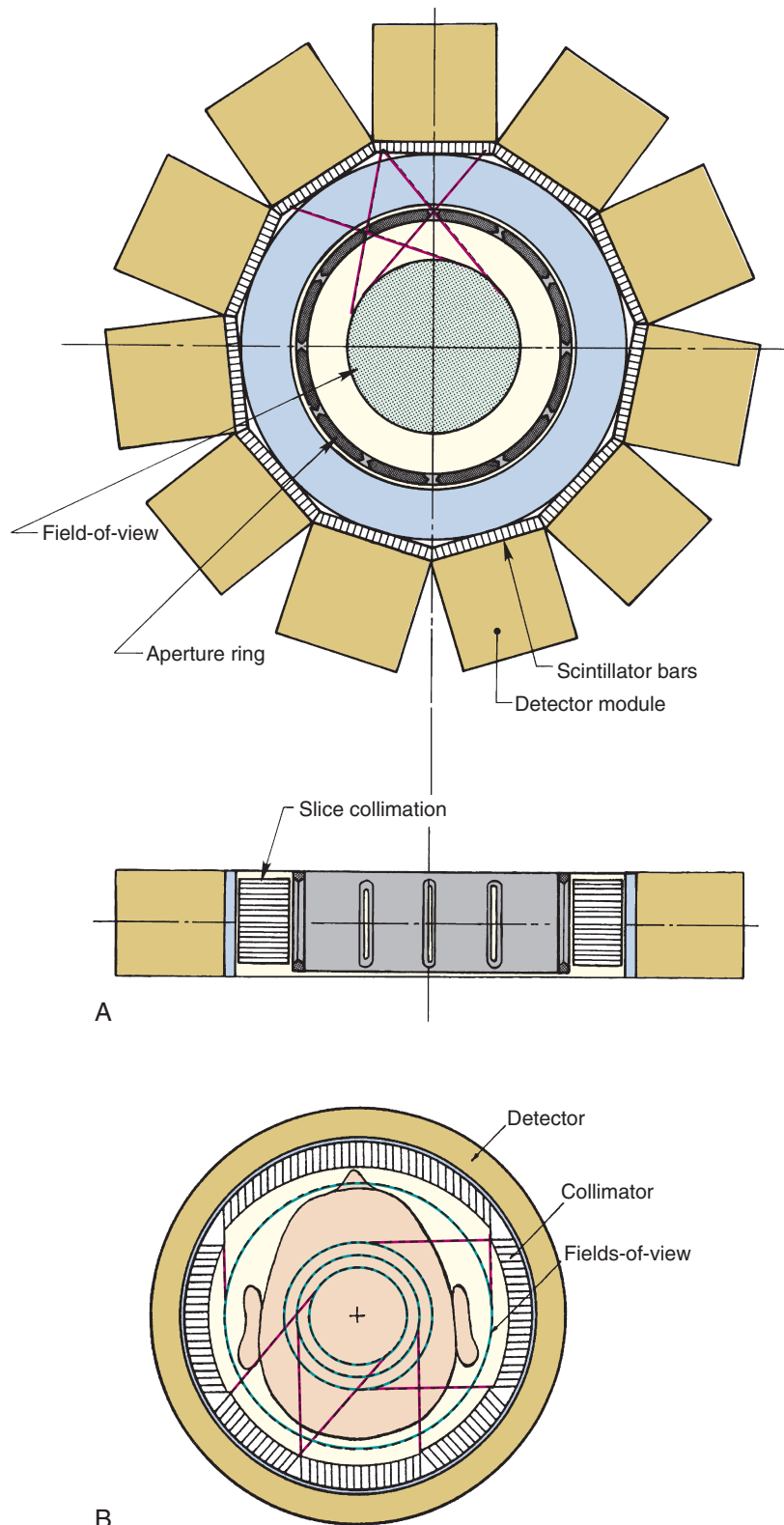
FIGURE 17-2 Cross-sectional views showing the design of two SPECT systems designed for brain imaging. *A,* The SPRINT system developed at the University of Michigan. This system employs a rotating collimator with 12 axial slits. Transverse and axial views are shown. *B,* The CERASPECT system developed by Digital Scintigraphics, Inc., Cambridge, MA. In this system, each collimator segment has a different field-of-view diameter. (*A, From Rogers WL, Clinthorne NH, Shao L, et al: SPRINT II: A second-generation single-photon ring tomograph.* IEEE Trans Med Imag *7:291-297, 1988; B, From Genna S, Smith AP: The development of ASPECT, an annular single-crystal brain camera for high-efficiency SPECT.* IEEE Trans Nucl Sci *35: 654-658, 1988.)*
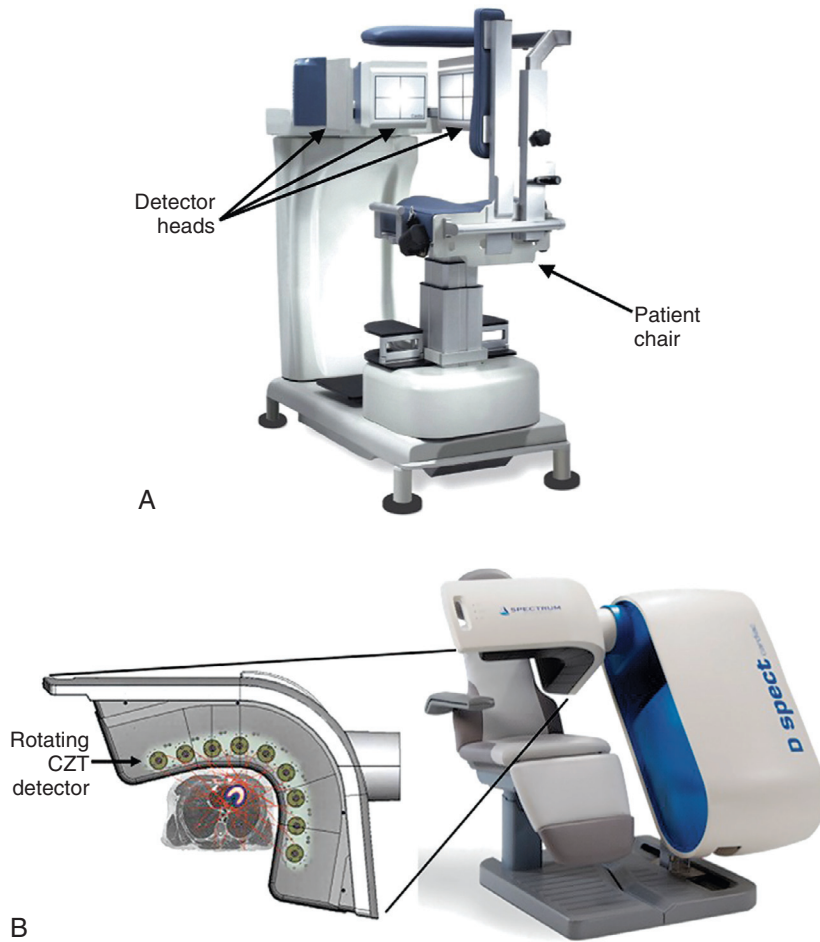
FIGURE 17-3 Photographs of dedicated cardiac SPECT scanners: *A,* A system with three detector heads. The patient sits upright in the chair and the chair rotates in front of the detectors to acquire the projection angles necessary for tomographic reconstruction. *B,* A system comprising nine cadmium zinc telluride detector heads arranged in an arc around the patient. Each detector head rotates independently to provide different angular views. The patient remains stationary in the chair. (*A, Courtesy Digirad Corp., Poway, CA; B, Courtesy Spectrum Dynamics Ltd. Caesarea, Israel.*)

rotates in front of an arc-shaped gamma camera that employs traditional continuous NaI(Tl) crystals read out by PM tubes.[5] This rotating collimator gives rise to the different projection angles, with slice collimation provided by a stationary stack of thin concentric lead rings. For a source-to-aperture distance of 20 cm, this system can provide reconstructed spatial resolution in the range of 6 to 7 mm.

4. SPECT Systems for Small-Animal Imaging

In addition to their widespread clinical role, SPECT systems also are used for applications in biomedical research involving small animals. Typical applications are the

evaluation of new radiopharmaceuticals being developed for diagnostic purposes, or the use of established radiopharmaceuticals to measure functional, physiologic, or metabolic processes in an animal model to monitor or understand the response to a new therapeutic approach.

The challenge is the small size of the organs (a few millimeters in diameter) in commonly used experimental animals such as mice and rats, relative to the spatial resolution typically obtained with SPECT systems. However, two key factors can be exploited to obtain much higher spatial resolution with SPECT in small animals compared with what can be achieved in human imaging. The first is the small volume of tissue to be imaged, which, depending on the detector size used, can

permit high magnification of the object onto the detector with pinhole or converging hole collimators (see Fig. 13-7). The second related factor is that the organ of interest can always be positioned within a few millimeters (rather than many centimeters in humans) of the collimator. Because of the strong dependence of spatial resolution on source-to-collimator distance (see Fig. 14-16), much higher resolution can therefore be obtained. Furthermore, if pinhole collimation is used, the sensitivity also increases rapidly as objects of interest are moved close to the pinhole aperture (see Fig. 14-21B and Equation 14-16).

Thus the most common approach to small-animal imaging with SPECT has been to use pinhole collimation, with some magnification. Indeed, standard clinical SPECT systems have been used to great effect in small-animal imaging using a pinhole or multipinhole collimator. However, to achieve optimal resolution and sensitivity performance, in a compact device suited to a laboratory environment, dedicated small-animal SPECT systems have been developed. Although there are many different designs, these systems commonly consist of a series of compact detector heads, with interchangeable pinhole collimators that have apertures ranging from approximately 0.3 mm to 2 mm in diameter, allowing the operator to trade off between improved spatial resolution (smaller pinholes) or improved sensitivity (larger pinholes) (see Equations 14-15 and 14-16). The detector heads often use pixelated NaI(Tl) or CsI(Tl) scintillator arrays (similar to those shown in Fig. 13-15B) or arrays of CZT semiconductor elements to achieve high intrinsic spatial resolution. The simplest systems consist of two opposing detector heads, each with a single pinhole collimator, that rotate around the animal and translate along the animal to produce the angular projections required for reconstruction tomography.

More advanced systems employ collimators with multiple pinholes to improve sensitivity. Such collimators also can increase the FOV along the axial direction without the need to translate the animal. In the most straightforward implementation, the pinholes are arranged with sufficient distance between them such that the image of the animal projected through adjacent pinholes does not overlap on the detector (Fig. 17-4, *left*). In some systems, the projections are allowed to overlap to a certain degree, which enables more pinholes to be used for a given detector area and magnification (Fig. 17-4, *right*). However, this leads to ambiguity in the projection data in the region of overlap, and tomographic reconstruction into SPECT images must use algorithms that properly model this ambiguity.

Some multipinhole animal SPECT systems are completely stationary and designed such that they simultaneously acquire sufficient angular data for tomographic reconstruction with no moving parts. This type of system is particularly suited for rapid dynamic studies, often of interest when evaluating the biodistribution of a novel radiotracer in the first seconds and minutes after injection. These systems consist of an annular collimator sleeve containing many pinholes each projecting a different angular view of the radionuclide distribution onto a detector that sits behind the collimator. Figure 17-5 shows one such collimator and a drawing showing how
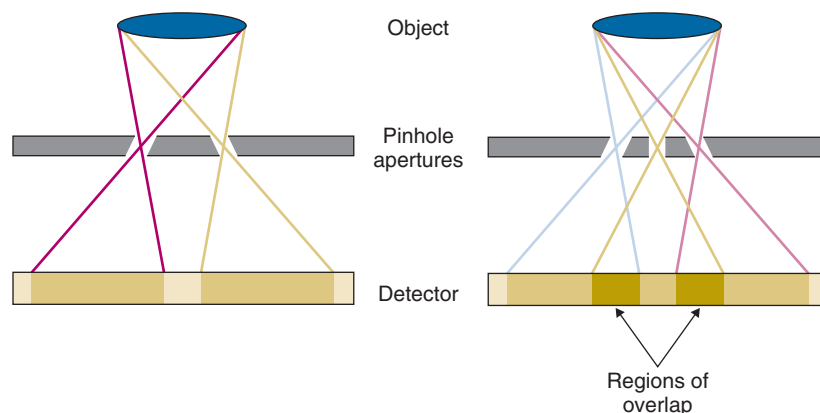

FIGURE 17-4 Illustration of multiple pinhole systems used for small-animal SPECT. *Left,* Two pinholes spaced far enough apart to avoid overlap of projections. *Right,* Increased number of pinholes provides increased sensitivity, but comes at the expense of a partial overlap in the projection data viewed through adjacent pinholes.
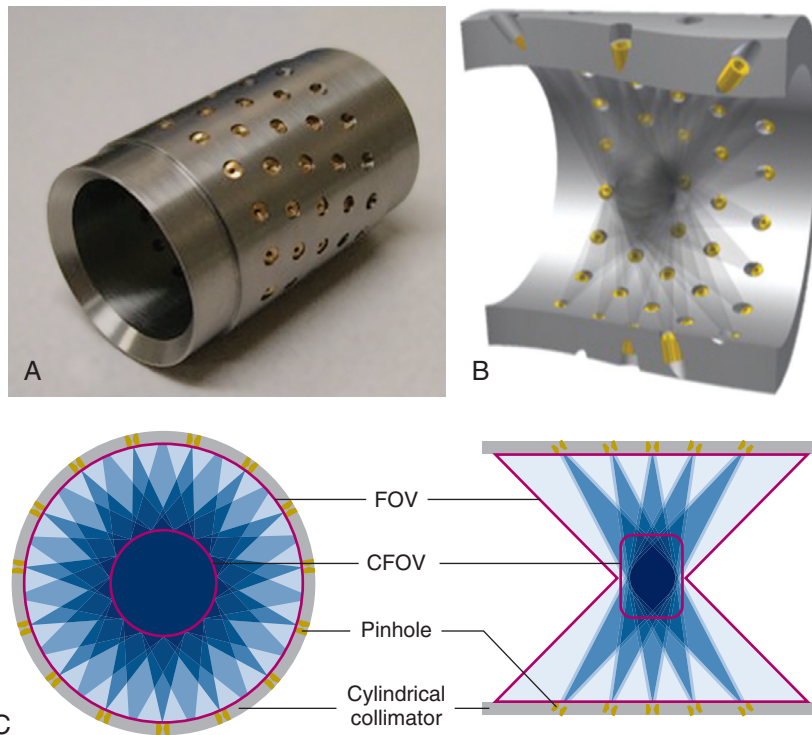
FIGURE 17-5 *A,* Photograph of multiple-pinhole collimator for a stationary small-animal SPECT system. There are 75 pinholes viewing the object from different angles. *B,* Cut-away view of the pinhole collimator showing angulation of pinholes and dense sampling in the central region. *C,* Transverse and axial sections through the center of the collimator showing sensitive region for each pinhole and extent of field of view. (*Courtesy MILabs, Utrecht, The Netherlands*).

the pinholes are angled to cover a large FOV without the need for any movement.

Using these approaches, small-animal SPECT systems routinely reach a resolution in the range of 1 mm, and in some instances are able to produce images with a reconstructed resolution much smaller than 1 mm. Sensitivity can be high as well, because of the large number of pinholes used. Numbers are commonly in the 0.5 to 2 $\times$ 10³ cps/MBq (~1000-4000 cpm/µCi) range, but depend strongly on the number and diameter of the pinhole apertures used, and the source-to-pinhole distance. For systems in which the projections overlap, the measured sensitivity must be interpreted with caution, as the information content of an event detected in a region of overlap is not as high as for an event in a system in which the projections do not overlap. Almost all small-animal systems use some form of iterative reconstruction algorithm with detailed modeling of the collimator apertures for reconstructing images at the highest possible resolution. Figures 17-6A and B show photographs of two SPECT systems designed for small-animal imaging

applications. A useful review of small-animal SPECT systems is given in reference 6.

B. PRACTICAL IMPLEMENTATION OF SPECT

Ideally, the signal level for a voxel in a SPECT image is linearly proportional to the amount of activity contained within the volume of tissue in the patient that corresponded to the location of that voxel. This would be useful not only for quantitative applications, such as perfusion studies, but also for visual interpretations of the image. In practice, this ideal result is not achieved because the realities of data acquisition do not match the idealized assumptions made for the development of reconstruction algorithms. As shown in Figure 16-1, it was assumed that the line of response (or a projection element) for a single hole in a parallel-hole collimator is an extended cylinder, but the actual response resembles a diverging cone. It was further assumed that the signal recorded was proportional to the total activity within the line of response, but
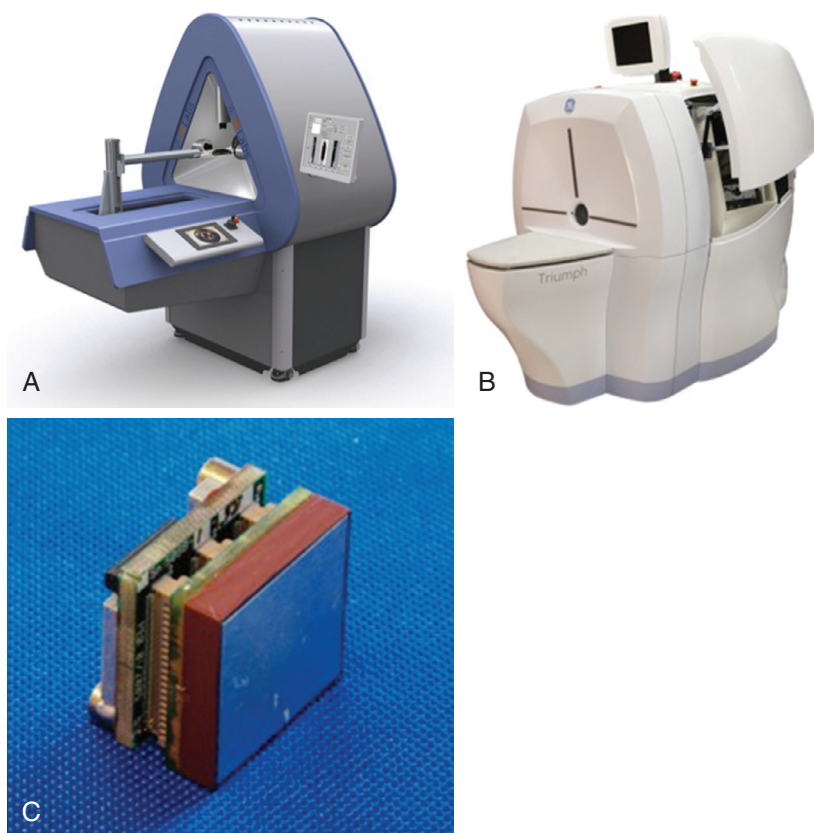
FIGURE 17-6   Photographs of two small-animal SPECT systems: *A,* This stationary system uses the cylindrical multi-pinhole collimator shown in Figure 17-5, and views are projected onto three large-area Anger cameras with no overlap between projections. With no need to move the detectors, fast dynamic studies can be performed. *B,* This system employs four 12.7 cm × 12.7 cm pixelated cadmium zinc telluride (CZT) detector heads and multipinhole collimators. Some rotation of the detectors is necessary to obtain all projection angles. The use of CZT provides excellent energy resolution. *C,* Photograph of one detector module from the system shown in B. The detector measures 2.54 cm × 2.54 cm and has a 16 × 16 array of CZT elements on a 1.59-mm pitch. The CZT thickness is 5 mm. Twenty-five of these modules are tiled together to form a 12.7 cm × 12.7 cm detector head. (*A, Courtesy MILabs, Utrecht, The Netherlands; B, Copyright Gamma Medica, Northridge, CA and GE Healthcare, Waukesha, WI; used with permission of GE Healthcare; C, Copyright Gamma Medica, Northridge, CA.)*

in fact the signal from activity closest to the detector is more heavily weighted than from deeper-lying activity, because of attenuation by overlying tissues. Finally, it was assumed that activity outside the line of response did not contribute to the signal for the projection element, whereas there may be crosstalk between elements resulting from scattered radiation or septal penetration through the collimator. To further complicate matters, most of the discrepancies vary with the energy of the γ rays involved.

Some of the discrepancies between the idealized assumptions and the actual situation in SPECT are illustrated in Figure 17-7. The discrepancies distort the desired linear relationship between signal level and amount of activity present. They also can lead to artifacts and seriously degraded image quality. To avoid this, one must use somewhat modified approaches to data acquisition or apply post-processing of the acquired data. This is always the case when backprojection algorithms are used, because they are rigorously grounded in the idealized assumptions noted earlier. Some of the discrepancies can be accounted for with iterative algorithms, such as the maximum likelihood-expectation maximization algorithm (see Chapter 16, Section D.2), which can incorporate these factors in its probability matrix. In this section, we describe some general approaches that are valid and potentially useful for all reconstruction algorithms.
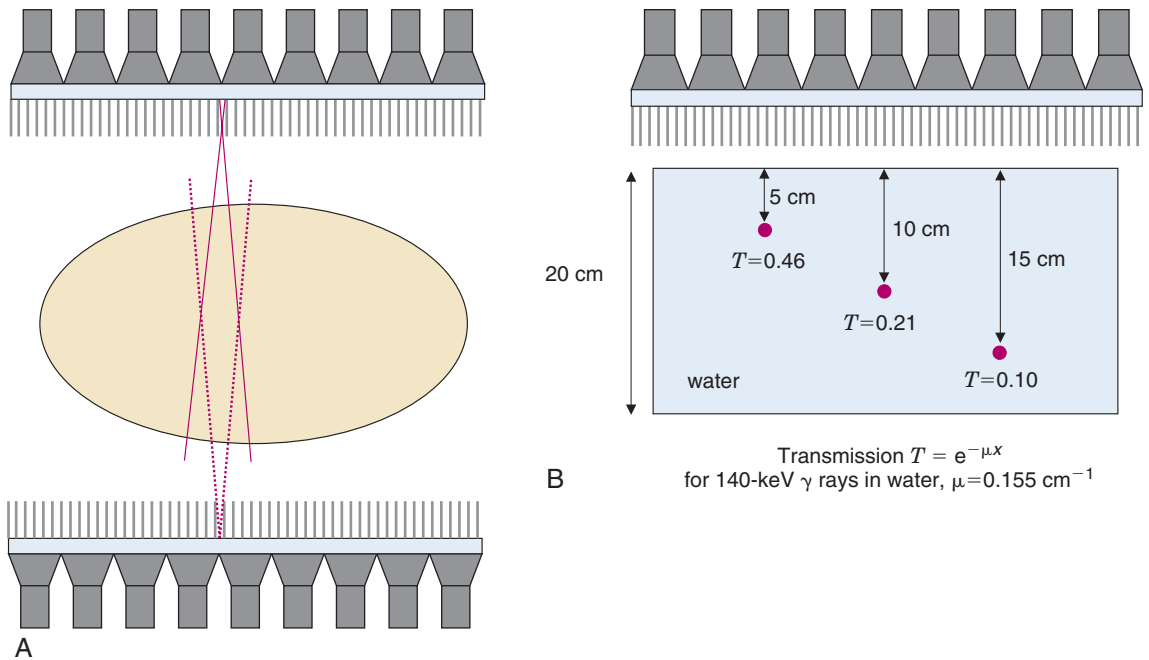
FIGURE 17-7   *A,* Volumes of tissue viewed by a collimator hole at two different angles separated by 180 degrees. Differences in the volumes viewed results in different projections from the two viewing angles. *B,* Attenuation leads to further differences in these two projections, emphasizing activity that is close to the gamma camera compared with activity further away that has to penetrate more tissue to reach the gamma camera. Values are shown for the attenuation of the 140-keV γ rays from ^{99m}Tc in water.

1. Attenuation Effects and Conjugate Counting

The attenuation of γ rays in SPECT imaging depends on the distance the γ rays have to travel through the tissue to reach the detector. Figure 17-7B illustrates the depth-dependent nature of this attenuation for point sources located at different positions within the body. The transmission factor for a source at a certain depth can be calculated using Equation 6-22. For 140-keV γ rays, the linear attenuation coefficient of tissue is 0.155 cm^{-1}; therefore γ rays that are emitted from a depth of 10 cm in the body would only have a probability of 0.21 ($e^{-10 \times 0.155}$) of emerging from the body in their original direction. The attenuation of γ rays is even more severe in parts of the body containing significant amounts of bone, because the linear attenuation coefficient of bone is ~0.25 cm^{-1} at 140 keV.

One approach to reducing both the divergence of the response profile (Fig. 17-7A) and the effects of tissue attenuation (Fig. 17-7B) is conjugate counting. *Conjugate counting* refers to acquiring data (or image profiles) for directly opposing views and then combining these data into a single dataset or line of response. A source that is located relatively close to the detector from one view will be relatively far away in the opposing view. Hence, the response profile will be narrower and attenuation by overlying tissues will be smaller in the first view and larger in the second, with partially offsetting effects.

Conjugate counting in SPECT requires that views be obtained over a full 360-degree range around the object. Data from opposing views then are combined to yield the equivalent of a single 180-degree scan. Conjugate counts (or views) generally are combined in one of two ways. The first is to use the *arithmetic mean.* If I_1 and I_2 are the counts recorded from opposing directions for a particular line of response through the object, the arithmetic mean is given by

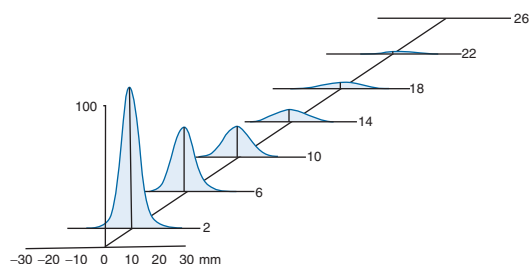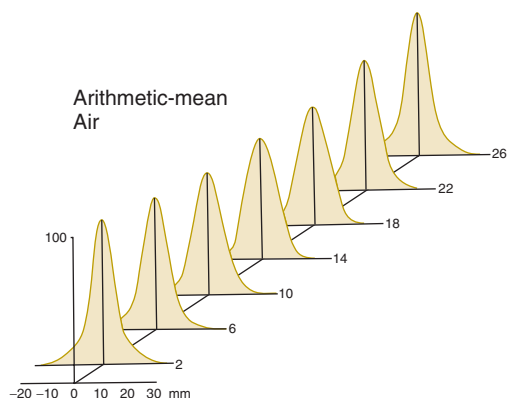$$\overline{I}_A = \frac{(I_1 + I_2)}{2} \qquad (17\text{-}1)$$

An alternative is the *geometric mean,* given by

$$\overline{I}_G = \sqrt{I_1 \times I_2} \qquad (17\text{-}2)$$
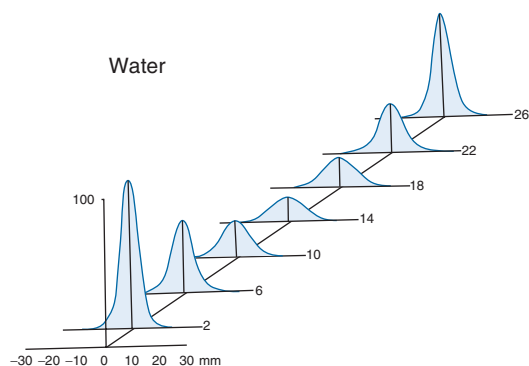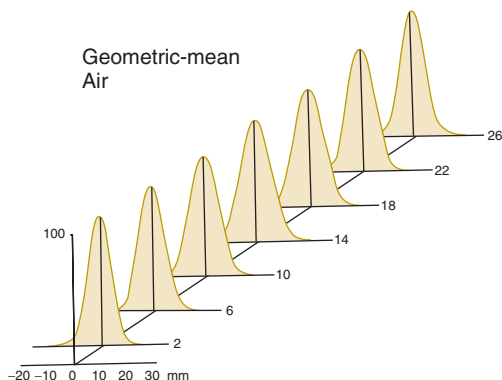
Figure 17-8 shows response profiles versus source depth for a ^{99m}Tc line source for a single-view projection and for projections
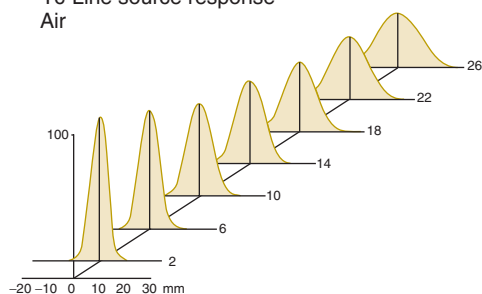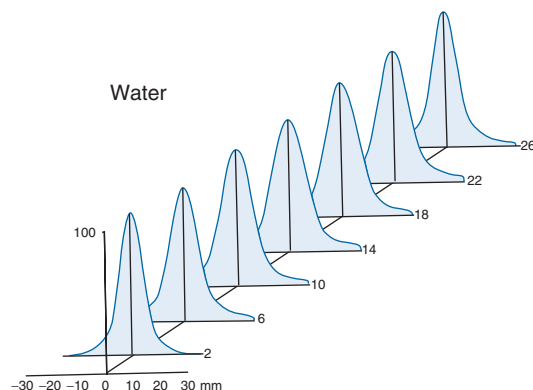
FIGURE 17-8 Line-spread functions versus distance in air (*left*) and in water (*right*) for high-resolution parallel-hole collimator on a gamma camera. The line source measured 2.5 mm in diameter and was mounted inside a tank measuring 410 mm in length, 310 mm in width, and 300 mm in thickness. Measurements were made either with the tank empty (in air) or filled with water. *Top,* single detector only; *middle,* arithmetic mean of opposing detector profiles; *bottom,* geometric mean of opposed detector profiles. (*From Larsson SA: Gamma camera emission tomography: Development and properties of a multisectional emission computed tomography system.* Acta Radiol Suppl *363:1-75, 1980.*)

created from the arithmetic and geometric means of opposing views. The profiles across the top are for a single view with the source in air and for the same view with the source in water. The profile for the source in air illustrates the degradation of spatial

resolution with distance from the collimator that is characteristic for a parallel-hole collimator (see also Figs. 14-18 and 14-19). The profile for the source in water shows similar degradation of spatial resolution with increasing distance but, in addition, shows

decreasing amplitude of response owing to attenuation of photons by the overlying thickness of water.

The middle row of Figure 17-8 shows response profiles for the arithmetic mean. The profiles for the source in air show significantly improved uniformity of spatial resolution with depth, as compared with the single-view profile directly above it. The profiles for the source in water show similar improvement in uniformity of spatial resolution with depth; however, there still is marked variation in the amplitude of the profile versus distance (and depth in water), indicating that the effects of photon attenuation are only partially corrected for by the arithmetic mean.

The response profile for the arithmetic mean has its minimum amplitude when the source is near the center of the water phantom. Figure 17-9 shows simulated SPECT images of a water-filled cylinder containing a solution of uniform concentration of activity for different γ-ray energies, using the arithmetic mean of opposing views. Also shown are profiles of the images across the center of the phantom. As one might expect from the profiles illustrated in Figure 17-8, there is a marked decrease in intensity at the center of the
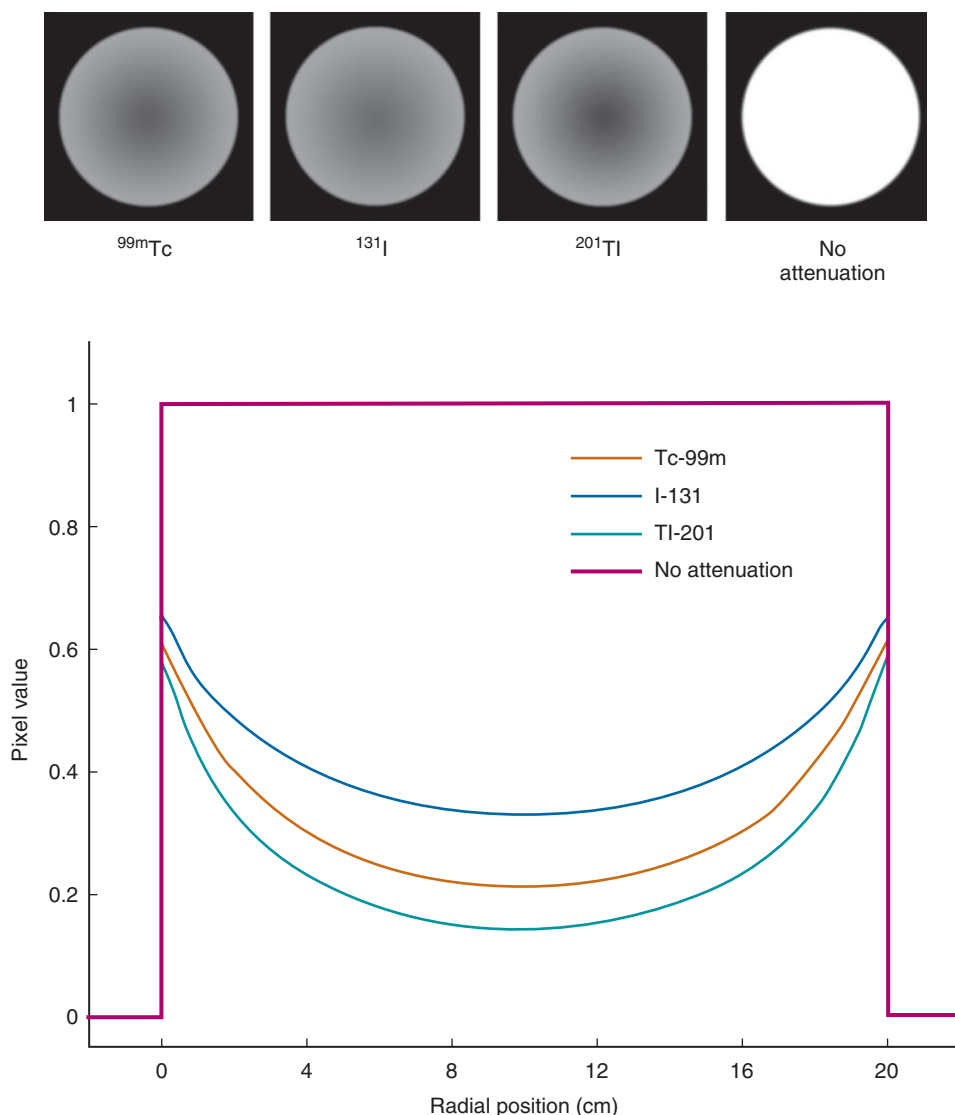
FIGURE 17-9 *Top,* Simulated SPECT images of 20-cm diameter water-filled cylinders containing uniform concentrations of ^{99m}Tc (140 keV), ^{131}I (364 keV), and ^{201}Tl (70 keV). *Bottom,* Arithmetic mean of count profiles through the center of the simulated images. Note the reduction in image intensity at all points in the image caused by attenuation, with the largest reduction occurring at the center of the cylinder. The amount of attenuation is energy dependent, with greatest attenuation occurring at the lower γ-ray energies.

phantom. The strongest effect occurs for the lowest energy γ rays. It is apparent from Figure 17-9 that relatively strong attenuation effects are present with the arithmetic mean for all of the photon energies commonly used in SPECT imaging.

Figure 17-10 shows simulated images and profiles for phantoms of different sizes with $\mu = 0.155$ cm^{-1}, corresponding to the attenuation of 140-keV photons of ^{99m}Tc in water. As the diameter of the phantom increases, the images and count profiles demonstrate progressively greater suppression at the center of the image.

The bottom row of Figure 17-8 shows profiles in air and in water for the geometric mean of opposing views. In this case, both the amplitude and the width of the profile remains nearly constant at all distances and depths in the water phantom.

Tables 17-1 and 17-2 summarize numerical data derived from the profiles in Figure 17-8. From this summary, it can be seen that attenuation has much stronger effects than distance. The combined effects of distance and attenuation result in a 100-fold range in counts recorded with a single detector (see Fig. 17-8, *top right*). With the arithmetic

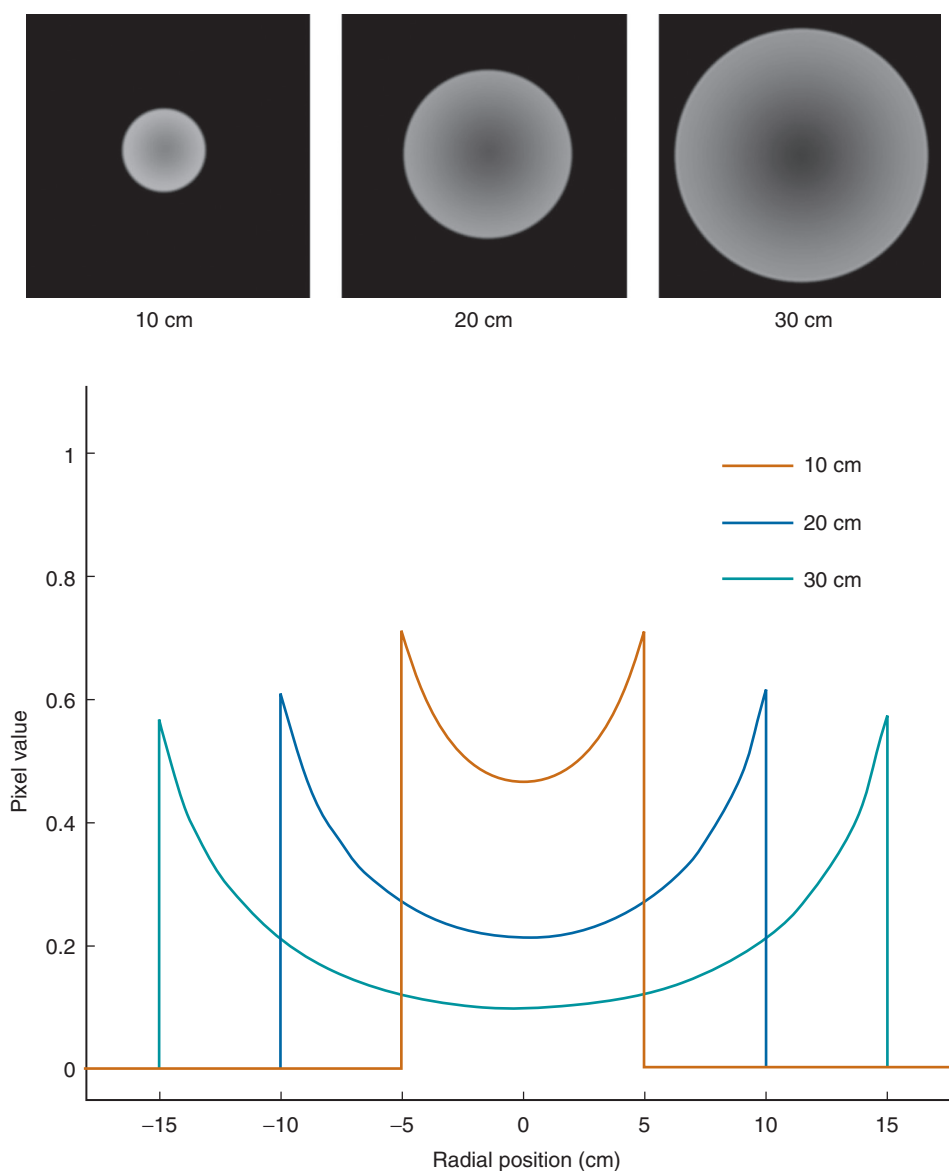**FIGURE 17-10** *Top,* Simulated SPECT images of water-filled cylinders of different diameters containing uniform concentrations of ^{99m}Tc (140 keV). *Bottom,* Count profiles through the centers of the images. The strong dependence of attenuation on cylinder size is evident.

TABLE 17-1
NUMERICAL DATA FOR FIGURE 17-8 (LEFT COLUMN) ^{99m}Tc LINE SOURCE IN AIR

	Distance from Collimator (cm)	Relative Maximum Response* in Air (%)	Resolution FWHM (mm)
^{99m}Tc line-source response	2	100	7.4
	6	84	8.6
	10	66	10.0
	14	58	12.5
	18	49	14.7
	22	44	17.2
	26	38	20.0
Arithmetic mean	2-28†	100	8.5
	6-24	93	10.6
	10-20	84	12.3
	14-16	84	13.2
	18-12	82	12.7
	22-8	90	11.2
	26-4	99	9.8
Geometric mean	2-28	100	9.4
	6-24	98	10.8
	10-20	94	12.4
	14-16	94	13.2
	18-12	93	12.7
	22-8	97	11.7
	26-4	100	10.4

Adapted from Larsson SA: Gamma camera emission tomography: Development and properties of a multisectional emission computed tomography system. *Acta Radiol Suppl* 363:1-75, 1980.

FWHM, full width at half maximum.

*Value at peak of profile.

†For arithmetic and geometric means, paired values refer to the distance between the source and collimator for the two conjugate views.

mean (see Fig. 17-8, *middle*), the range is reduced to a factor of five. With the geometric mean (see Fig. 17-8, *bottom*), the variations with depth are virtually eliminated, although there still is a small reduction in relative counts when the source is at the deepest location in the phantom.

The constancy of amplitude for the geometric mean can be understood from the following analysis. Consider the arrangement of the radioactive source and detectors shown in Figure 17-11. The attenuation of photons directed toward detector 1 is given by

$$I_1 = I_{01}(e^{-\mu a}) \qquad (17\text{-}3)$$

and for those directed toward detector 2 by

$$I_2 = I_{02}(e^{-\mu b}) \qquad (17\text{-}4)$$

where a and b are the source depths. Note that $a + b = D$. Taking the geometric mean of I_1 and I_2, one obtains

$$\sqrt{I_1 \times I_2} = \sqrt{(I_{01} \times I_{02})e^{-\mu \times (a+b)}}$$
$$= \sqrt{(I_{01} \times I_{02})}e^{-\mu D/2} \qquad (17\text{-}5)$$

Thus the geometric mean of counts from opposed detectors depends on total tissue thickness, D, but not on source depths, a and b. This result is exact only for a point or plane source, but corrections can be applied as approximations for simple extended sources (e.g., uniform volume sources).[7] The geometric mean also depends on the unattenuated counts, I_{01}, and I_{02}, which may change with a and b because of distance effects; however, for systems using parallel-hole collimators, such as SPECT gamma camera systems, unattenuated counts do not change with distance (see Chapter 14, Section C.3 and Fig. 14-17). In this case, $I_{01} = I_{02} = I_0$ and Equation 17-5 reduces to

$$\sqrt{I_1 \times I_2} = I_0 e^{-\mu D/2} \qquad (17\text{-}6)$$

TABLE 17-2
NUMERICAL DATA FOR FIGURE 17-8 *(RIGHT COLUMN)* ^{99m}Tc LINE SOURCE IN WATER

	Distance from Collimator (cm)	Relative Maximum Response* in Water (%)	Resolution FWHM (mm)
^{99m}Tc line-source response	2	100	7.5
	6	47	9.4
	10	23	11.2
	14	10	13.9
	18	8.1	16.3
	22	1.9	19.1
	26	0.8	21.6
Arithmetic mean	2-28[†]	100	7.8
	6-24	50	8.6
	10-20	25	11.5
	14-16	17	14.3
	18-12	21	13.0
	22-8	34	10.4
	26-4	71	8.1
Geometric mean	2-28	100	9.9
	6-24	93	11.7
	10-20	95	13.3
	14-16	93	14.3
	18-12	95	14.1
	22-8	93	13.2
	26-4	96	11.9

Adapted from Larsson SA: Gamma camera emission tomography: Development and properties of a multisectional emission computed tomography system. *Acta Radiol Suppl* 363:1-75, 1980.

FWHM, full width at half maximum.

*Value at peak of profile.

[†]For arithmetic and geometric means, paired values refer to the distance between the source and collimator for the two conjugate views.
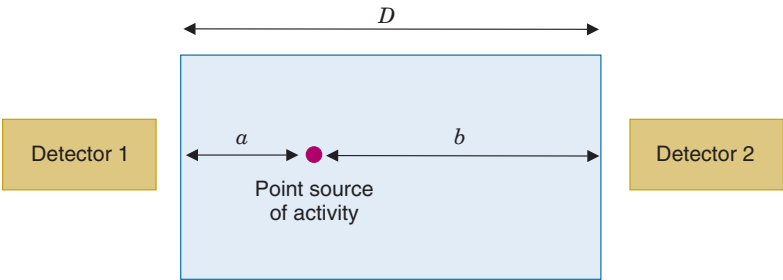

FIGURE 17-11   Point source of activity within an attenuating medium of thickness *D*. The attenuation can be compensated for by using the geometric or arithmetic mean and a correction for total tissue thickness, *D*.

These analyses and equations are accurate for a single radioactive source. When multiple sources are present, the situation is more complicated, as shown in Example 17-1.

EXAMPLE 17-1

Derive the equation for the geometric mean of counts from two point sources located along a line between two detectors, and show why it cannot be described only in terms of the unattenuated counts, I_{01}, and I_{02}, and μ and D (distance between the detectors) as can be done for a single point source (Equation 17-5). Assume that a parallel-hole collimator is being used and therefore that the unattenuated counts do not depend on distance.

Answer
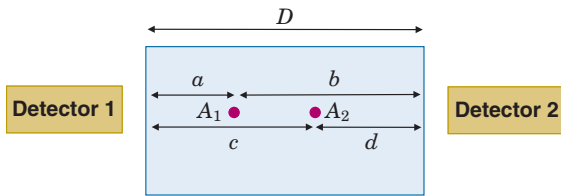
Referring to this figure:

$$a + b = D$$

$$c + d = D$$

We represent the unattenuated counts from source A_1 as I_{01} and from source A_2 as I_{02}. The measured counts at detector 1 will be

$$I_1 = I_{01}e^{-\mu a} + I_{02}e^{-\mu c}$$

The measured counts at detector 2 will be

$$I_2 = I_{01}e^{-\mu b} + I_{02}e^{-\mu d}$$

The geometric mean is

$$\sqrt{I_1 \times I_2} = \left[I_{01}^2 e^{-\mu(a+b)} + I_{02}^2 e^{-\mu(c+d)} + I_{01}I_{02}e^{-\mu(a+d)} \right.$$
$$\left. + I_{01}I_{02}e^{-\mu(c+b)} \right]^{1/2}$$
$$= \left[\left(I_{01}^2 + I_{02}^2 \right)e^{-\mu D} + I_{01}I_{02}e^{-\mu(a+d)} \right.$$
$$\left. + I_{01}I_{02}e^{-\mu(c+b)} \right]^{1/2}$$

Only the first term in the last expression depends solely on I_{01}, I_{02}, μ, and D. The other two terms contain exponential terms $e^{-\mu(c+b)}$ and $e^{-\mu(a+d)}$ that depend on the relative locations of the two sources between the detectors. Therefore attenuation effects depend on the source distribution, and the simple correction scheme for point sources and line sources must be modified for more complicated source distributions.[7]

2. Attenuation Correction

Conjugate-counting techniques, especially using the geometric mean, can substantially reduce the variation of width and amplitude of counting rate profiles that are present in single-view profiles. However, even with the geometric mean, there are residual scaling factors caused by attenuation [exp(−μD/2) in Equation 17-6]. Thus, for quantitative accuracy, attenuation corrections are required.

A relatively simple method for attenuation correction is to correct projection profiles generated with the geometric or arithmetic mean before reconstruction using an estimate for tissue thickness, D. The attenuation correction is particularly simple for the geometric mean (Equation 17-6) and is given by multiplying the projection profiles by an attenuation correction factor (ACF) of

$$ACF = \frac{1}{e^{-\mu D/2}} = e^{\mu D/2} \qquad (17\text{-}7)$$

A constant value for μ, the linear attenuation coefficient of tissue, is assumed. An estimate for tissue thickness D can be derived from a preliminary uncorrected image or by assuming a standard body size and shape.

As demonstrated in Example 17-1, simply generating profiles using the geometric mean does not correctly deal with attenuation in the general case in which γ rays are emitted at different locations in the FOV. An alternative approach is to calculate an ACF for each pixel after image reconstruction. In this method, an initial image, $f'(x,y)$, is reconstructed by filtered back-projection without any attenuation correction. The contours of this image are used to obtain an estimate of the attenuation path length through the tissue for all projection views. Once again, it is assumed that the linear attenuation coefficient at a given energy is constant for all body tissues. The ACF for each pixel (x,y) in the reconstructed image then is calculated by

$$ACF(x, y) = \frac{1}{\dfrac{1}{N}\displaystyle\sum_{i=1}^{N} e^{-\mu d_i}} \qquad (17\text{-}8)$$

where d_i is the attenuation path length for the pixel at projection view i and μ is the assumed constant value for the attenuation coefficient. The reconstructed image $f'(x,y)$ is corrected on

a pixel-by-pixel basis by multiplying it by the ACF

$$f(x, y) = f'(x, y) \times ACF(x, y) \quad (17\text{-}9)$$

This technique is known as *Chang's multiplicative method.*[8]

There also is a more involved implementation of the Chang method in which the image obtained with the first-order correction described by Equation 17-8 is forward-projected (see Chapter 16, Section D.1), with appropriate attenuation of the image counts corresponding to the path length through the tissue.[9] The forward-projected profiles $p_{fp}(r, \phi)$ are subtracted from the original measured projection profiles $p(r, \phi)$ to form an "error projection" $P_{error}(r, \phi)$

$$P_{error}(r, \phi) = p(r, \phi) - p_{fp}(r, \phi) \quad (17\text{-}10)$$

This error projection is itself reconstructed with filtered backprojection to form an error image, $f_{error}(x,y)$. The final attenuation corrected image is given by

$$\begin{aligned} f(x, y) = {} & f'(x, y) \times ACF(x, y) \\ & + f_{error}(x, y) \times ACF(x, y) \end{aligned}$$

$$(17\text{-}11)$$

Adding the two images together is made possible by the fact that filtered backprojection is a linear algorithm. Figure 17-12 shows

No attenuation correction

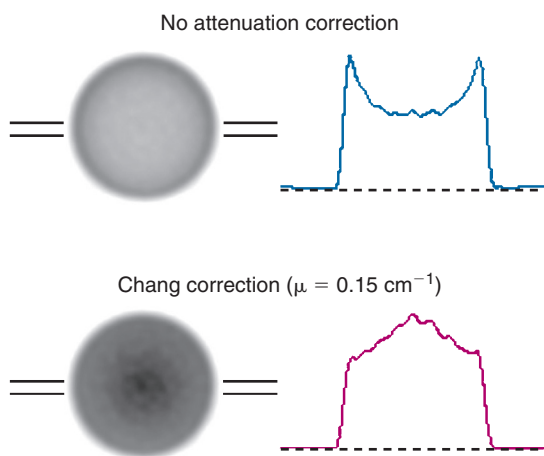Chang correction (μ = 0.15 cm^{-1})

FIGURE 17-12 SPECT images of a 20-cm diameter cylinder containing a uniform concentration of ^{99m}Tc with and without attenuation correction (Chang method with narrow-beam attenuation coefficient of μ = 0.15 cm^{-1}). Profiles are through the center of the images. The apparent overcorrection of attenuation is due to scattered events in the dataset. (*Courtesy Dr. Freek Beekman, Delft University of Technology, The Netherlands.*)

SPECT images of a cylinder that contains a uniform concentration of radionuclide before and after attenuation correction with the Chang method.

Methods based on the Chang approach are used in most commercial SPECT systems and yield reasonable results in the brain and abdomen, where the assumption of a uniform attenuation coefficient is not unreasonable (the amount of bone and any air spaces are small). These methods do not work well in the thorax or in the pelvic region, where the presence of the lungs and significant amounts of bone, respectively, can lead to significant errors. SPECT projection profiles must be acquired over a full 360 degrees to use these methods.

3. Transmission Scans and Attenuation Maps

An alternative approach for SPECT imaging in regions of the body that have variable attenuation is to actually measure tissue attenuation using an additional scan known as a *transmission scan.*[10,11] This scan can be performed using the same detector system as is used for acquiring the emission data. An external source of radiation is used to acquire transmission profiles that can be used to reconstruct cross-sectional images reflecting the linear attenuation coefficient of the tissue, often referred to as an *attenuation map*. This is equivalent to an x-ray CT scan, although the quality of the image is poorer, because of the limited resolution of the gamma camera and the low-photon flux used to obtain the transmission image. As well, the higher energy of the γ rays, as compared with most diagnostic x-ray beams, leads to lower contrast. Approaches that use x-ray CT scans for attenuation correction are discussed in Chapter 19, Section E.

Transmission data can be acquired using a collimated flood source, line source, multiple line sources, or a moving line source. Several possible acquisition geometries for transmission scans are shown in Figure 17-13. The data usually are acquired with a parallel-hole collimator on the detector, although on triple-headed cameras, a single line source sometimes is used in conjunction with a fan-beam collimator. The radionuclide chosen for the transmission sources usually has an emission energy that is different from ^{99m}Tc, to allow for simultaneous emission imaging of ^{99m}Tc, as described later. A radionuclide with a long half-life is convenient so that the source does
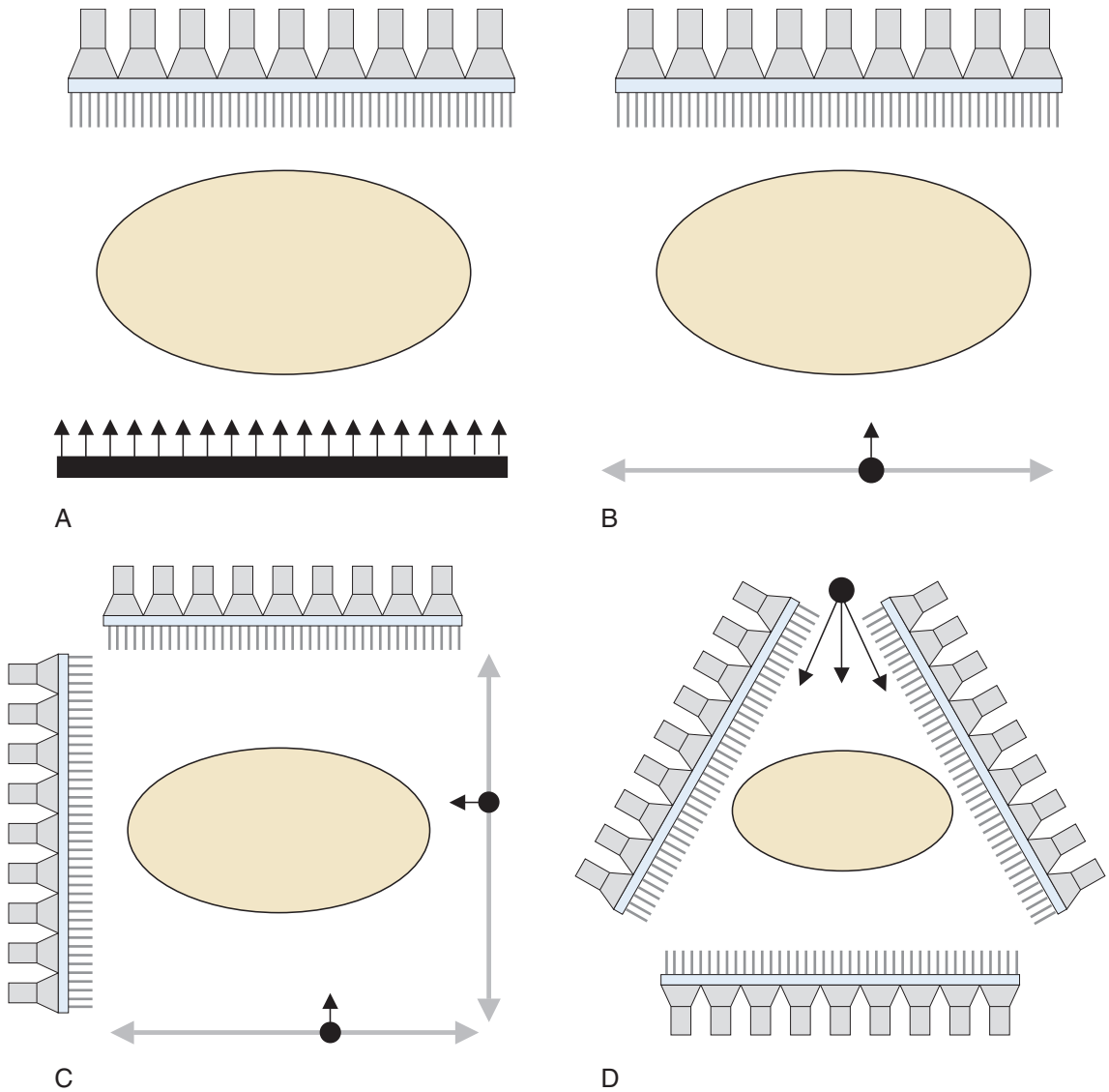
FIGURE 17-13 Examples of transmission source geometries that are being employed for attenuation correction in SPECT. The *black arrows* show the direction of γ rays emitted from collimated transmission source; the *gray arrows* show the direction of motion of moving line sources. *A,* Flood source. *B,* Collimated moving line source. *C,* Two orthogonal moving collimated line sources on dual-headed gamma camera. *D,* Stationary line source (collimated in axial direction irradiating opposite detector head (fan-beam collimator) in a triple-headed gamma camera.

not require frequent replacement. ^{153}Gd ($T_{1/2}$ = 242 days, E_γ = 97 and 103 keV) and ^{123m}Te ($T_{1/2}$ = 120 days, E_γ = 159 keV) are among the radionuclides suitable for this purpose.

To obtain an attenuation map, two separate scans are acquired with the transmission source. Typically one of the geometries shown in Figure 17-13 is used and the gamma camera system is rotated through 360 degrees to acquire a full set of projection views. The first scan is acquired with no object in the FOV of the SPECT camera. This is referred to as the *blank* or *reference scan*. The second

scan is acquired with the object of interest in the FOV. This is the transmission scan. The relationship between the reference (I_{ref}) and transmission (I_{trans}) counts in any particular projection element is given by the usual exponential relationship for γ-ray attenuation

$$I_{trans} = I_{ref}e^{-\mu x} \qquad (17\text{-}12)$$

Taking the natural logarithm of the ratio of the two scans results in

$$\ln(I_{ref}/I_{trans}) = \mu x \qquad (17\text{-}13)$$

Projection profiles of μx represent the sum of the attenuation coefficients along each line of response

$$\mu x = \sum_i \mu_i \Delta x_i \qquad (17\text{-}14)$$

where μ_i is the linear attenuation coefficient for the ith pixel and Δx_i is the pathlength of the line of response through the ith pixel. This is analogous to the standard emission projection profiles that represent the sum of the radioactivity along each line of response. Using the methods described in Chapter 16, Section B, the projection profiles of μx (calculated from the transmission scan profiles using Equation 17-13) are reconstructed, resulting in images of μ_i. Figure 17-14 shows a SPECT attenuation map reconstructed from transmission and reference scans.

The attenuation map can be used to more accurately compute the ACFs in the Chang algorithm (Section B.2) by taking into account the nonuniform attenuation at each source location in Equation 17-8. It can also be incorporated in the forward-projection step of the modified Chang algorithm to more accurately compute the error term. More commonly, tissue attenuation information is directly incorporated into iterative reconstruction algorithms (Chapter 16, Section D) in which it becomes another factor in the calculation of the probability matrix M in Equation 16-19. The probability for γ rays emitted from a given pixel i reaching projection element j is reduced by the probability of attenuation in the tissue lying between the point of emission and the detection point in the gamma camera. For both filtered backprojection and iterative algorithms, the difference in energy (and
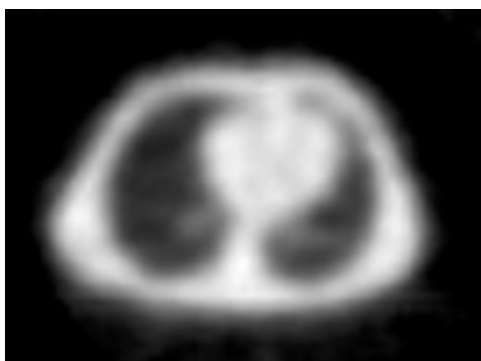

FIGURE 17-14 Attenuation map of the thorax reconstructed from the reference and transmission scans obtained with a moving line transmission source. (*Data courtesy Dr. Freek Beekman, Delft University of Technology, The Netherlands.*)

therefore attenuation) between the transmission and emission photons must be taken into account in applying the information from the transmission map.

Emission and transmission scans can be acquired simultaneously if the separation between the photon energies of the transmission source and the emission radionuclide is sufficient to allow them to be acquired in two separate energy windows. This is shown schematically in Figure 17-15. Even if two different windows are used, however, some events from the higher-energy radionuclide will be recorded in the lower-energy window. This effect, known as *downscatter*, arises from two causes. The first is spillover from higher-energy events into lower-energy regions of the spectrum (e.g., see Fig. 10-3). These events may arise from partial absorption of higher-energy photons in the detector or from natural broadening of the photopeak.

A second cause is γ rays that have experienced a partial loss of energy in Compton-scattering interactions in the body. For emission scans using ^{99m}Tc (140 keV), downscatter from a ^{123m}Te transmission source (159 keV) can appear in the emission source window. Conversely, when ^{153}Gd is used as the transmission source, downscatter from ^{99m}Tc can appear in the transmission source window. Even if the emission and transmission scans are acquired sequentially, rather than simultaneously, the patient normally is injected with a ^{99m}Tc-labeled radiopharmaceutical prior to transmission imaging, and hence downscatter is still an issue with ^{153}Gd transmission sources.

Downscatter can be estimated and corrections can be applied for it in ways that are similar to the methods used for correcting for scattered radiation in the emission scan. For example, one can use an energy window between the transmission and emission windows to estimate the level of downscatter. These methods are similar to those employed for scatter corrections, which are discussed in the following section.

4. Scatter Correction

The idealized model used for developing the filtered backprojection reconstruction algorithms described in Chapter 16 assumed that only radioactivity within the line of response for a projection element contributed to the signal for that element. In practice, the signal can include events that have been scattered into the line of response from radioactivity elsewhere in the body. With the typical 20%
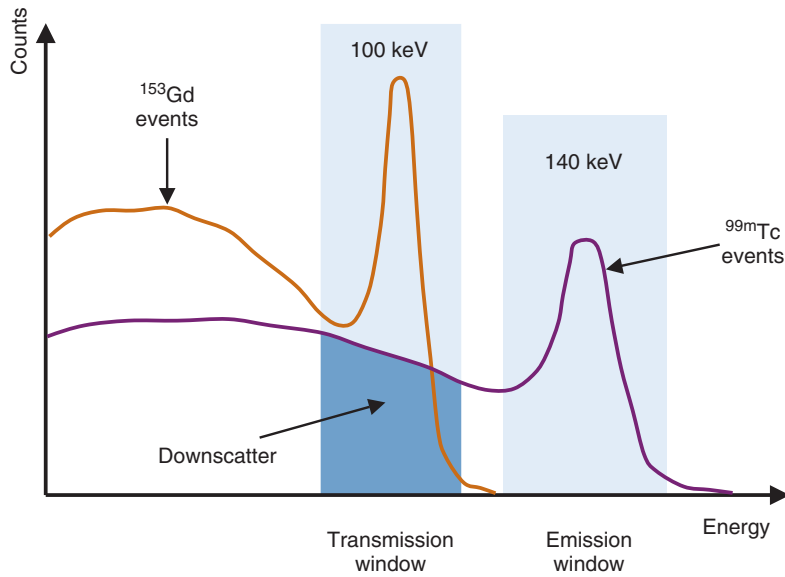
FIGURE 17-15 Dual-energy windows used to simultaneously acquire SPECT emission (^{99m}Tc) and transmission (^{153}Gd) data. Note the presence of downscatter from the ^{99m}Tc activity in the ^{153}Gd window. The magnitude of the downscatter contamination depends on the relative amounts of ^{99m}Tc activity in the body and ^{153}Gd activity in the transmission source, the amount of scattering material in the field of view, the details of how the transmission source is collimated, and the precise energy windows that are used.

pulse-height analyzer (PHA) window that is used for ^{99m}Tc, events that have scattered through angles as large as 50 degrees still have a 50% probability of being accepted.

Compared with the effects of attenuation, the effects of scattering are of lesser magnitude. Nevertheless, Compton scattering, and at low γ-ray energies ($\lesssim$100 keV) coherent scattering (see Chapter 6, Section C.5), still can have a significant effect on image quality and on the quantitative relationship between the reconstructed image intensity and source activity. In a typical patient study with a ^{99m}Tc-labeled radiopharmaceutical, even using a narrow 15% PHA window, the ratio of the number of detected scattered photons to the number of nonscattered photons may be as large as 40%. The presence of scattered events results in reduced image contrast (the tails of the point-spread function [PSF] are elevated with respect to the peak) and leads to an overestimation of the concentration of radioactivity in the pixel (see Fig. 17-12, *bottom*). The loss of image contrast may obscure clinically important details, particularly "cold" areas in the images, for example, areas of low radiopharmaceutical accumulation in the heart caused by coronary artery disease or infarction.

A first-order correction for scatter can be made by recognizing that scatter and attenuation are part of the same phenomenon. Attenuation is caused by the scattering (and

only rarely for energies $\gtrsim$100 keV, the total absorption) of γ rays. Because of the broad-beam geometry (Chapter 6, Sections D.2 and D.3) of SPECT imaging systems, some of the scattered γ rays are detected, leading, on average, to a reduction in the "apparent" attenuation coefficient that is measured relative to narrow-beam attenuation coefficients. One can provide an averaged correction for scatter by using the apparent or broad-beam value for μ in Equations 17-7 and 17-8. For example, for the 140-keV γ rays from ^{99m}Tc in a typical patient, the broad-beam attenuation coefficient is ~0.12 cm^{-1} as compared with a narrow-beam value of 0.155 cm^{-1}. Although this works well in objects with uniform radioactivity distributions in a uniform attenuation medium (Fig. 17-16), it does not properly
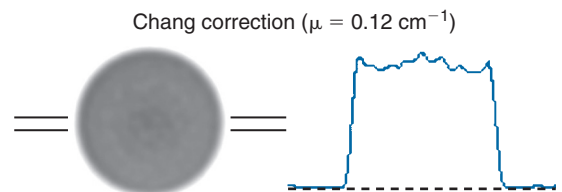
Chang correction ($\mu = 0.12$ cm^{-1})

FIGURE 17-16 Effect of Chang attenuation correction on 20-cm uniform cylinder data in Figure 17-12 using a broad-beam attenuation coefficient of $\mu = 0.12$ cm^{-1}. Note the improvement in the uniformity of the profile, which is due to compensation for scattered events. (*Data courtesy Dr. Freek Beekman, Delft University of Technology, The Netherlands.*)

take into account the spatial distribution of the scattered events and is therefore of limited accuracy in more realistic imaging situations.

A second simple method that has been used to correct for scattered events involves measuring the scatter component in the projection profiles using a line source (or point source) immersed in a scattering medium that is representative of the dimensions of the body. By measuring projection profiles of the source with and without the scattering medium, the distribution of scattered events in the projection profile can be determined. This can be considered to be the line-spread function (LSF) of the scattered events and can be deconvolved (see Appendix G) from the measured projection profiles measured in patient studies to correct for scatter. The accuracy of this correction is limited by differences in radioactivity distribution and attenuation distribution between the phantom in which the scatter response is measured, and the patient, and by the spatially invariant nature of the correction.

One of the most commonly used methods to correct for scattered γ rays is to simultaneously acquire counts with a photopeak window and a lower-energy *scatter window.* For example, the photopeak window for ⁹⁹ᵐTc might be set to 127-153 keV and the scatter window to 92-125 keV (Fig. 17-17). The resulting scatter projection profiles then are multiplied by a weighting factor and subtracted from the photopeak profiles to obtain scatter-corrected projection data. The weighting factor applied to the counts in the scatter window for the subtraction process must be determined experimentally and depends in general on the size of the source, the exact settings of the energy windows, and the energy resolution of the gamma camera detector. The accuracy of this method is limited by the fact that γ rays in the scatter window are more likely to have undergone multiple Compton interactions than scattered events in the photopeak window; therefore the spatial distributions of the scatter recorded in the two energy windows may differ.

Many variants on the use of multiple-energy windows for scatter correction have been developed. Some SPECT systems use as many as 32 separate energy windows to more accurately model the scatter distribution. Accurate scatter corrections require very good spatial linearity and uniformity of the gamma camera detector (Chapter 14, Section B) to avoid creating artifacts in the scatter correction process. Scatter corrections also increase the statistical noise in the reconstructed image because of the inevitable propagation of noise in the subtraction process (Chapter 9, Section C.1).

Note that for all the corrections described here, if scattered events are not "removed" prior to applying attenuation corrections, the scattered events also are amplified during the attenuation correction procedure. Therefore it is important that scatter corrections precede attenuation corrections.

Attenuation maps, described in the preceding section, also can be used in conjunction with iterative reconstruction algorithms to correct for scattered radiation. In essence, the matrix M in Equation 16-19 can be modified to account for the probability of scatter from a source at a location (x,y) into a specified detector element. This probability can be calculated by combining knowledge of the
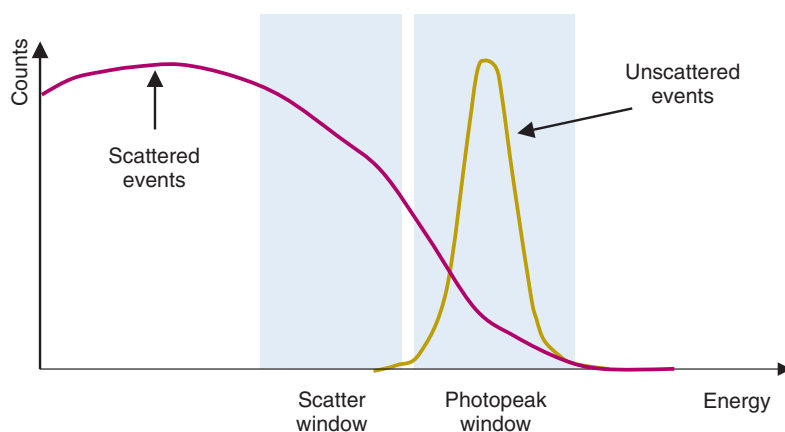

FIGURE 17-17 Diagrammatic sketch showing dual-energy windows superimposed on the spectral distribution of unscattered and scattered events for a patient-sized phantom filled with ⁹⁹ᵐTc.

distribution of the attenuation coefficients from the attenuation map, along with the probability of Compton scattering at different angles (see Fig. 6-13), and a model of the camera and collimator geometry, as well as the energy resolution of the camera.

Because computing the scatter probability from every source location in the subject, to every possible detector location, is computationally expensive, simplifying approximations often are made. Nonetheless, iterative algorithms in conjunction with patient-specific attenuation maps offer a powerful approach to quantitative SPECT imaging in the presence of nonuniform attenuating and scattering media. This is of particular value in cardiac imaging, in which the mixture of soft tissue and lungs in a cross-section of the thorax can cause major artifacts and quantitative errors if accurate corrections for attenuation and scatter are not employed. Scatter correction methods are discussed in more detail in reference 11.

5. Partial-Volume Effects

Ideally, the intensity of each pixel in a SPECT image would be proportional to the amount of radioactivity within the corresponding volume of tissue in the patient. The methods described in the preceding sections described how this can be facilitated by corrections for attenuation and scatter. Even with these corrections, however, there still may be errors in assigning activity and concentration values to small sources and small tissue volumes.

As described in Section C, a SPECT system has a characteristic "resolution volume" that is determined by the combination of its in-plane (x-y) and axial (z) resolutions. For systems that produce a stack of contiguous 2-D images, this volume has an approximately cylindrical shape of height = $2 \times$ FWHM axial resolution and diameter = $2 \times$ FWHM in-plane resolution. For sources or measurement volumes of the size of the resolution volume or larger, the intensity of images produced by the SPECT system reflect both the amount and concentration of activity within that volume. For smaller objects that only partially fill a resolution-volume element, the sum of the intensities of all the pixels that are attributable to that object still reflects the total amount of activity within it. However, the intensities of the individual pixels no longer accurately reflect the concentration of activity contained within them, because the signal is distributed over a volume that is larger than the actual size of the source. This

effect is illustrated in Figure 17-18, in which objects of identical concentration are seen to decrease in intensity, and thus in apparent concentration, with decreasing size.

This *partial-volume effect* is important for both qualitative and quantitative interpretation of SPECT images. Although they may be visible in the image, small objects near the resolution limits of the device appear to contain smaller concentrations of radioactivity than they actually do. The ratio of apparent concentration to true concentration is called the *recovery coefficient* (RC). Figure 17-19 illustrates RC versus object size for the cylinders in Figure 17-18. In principle, if a SPECT system has a known and uniform spatial resolution and if the size of the object is known, an RC correction factor can be applied to correct for the partial-volume underestimation of concentrations for small objects. Although this approach works well in phantom studies in which object sizes are well characterized, the sizes of in vivo objects usually are too poorly defined for this method to be useful, unless high-resolution anatomic information is available from another modality such as CT or magnetic resonance imaging.

In some situations, RC can be greater than one. This occurs when the object of interest has low radiotracer accumulation relative to surrounding structures (e.g., an area of reduced blood flow in the heart) and activity from these surrounding areas "spills over" into the structure of interest as a result of the same resolution effects described previously. This is commonly known as *spillover*. The net effect of partial-volume effects in all cases is to reduce the contrast between areas of high radiotracer uptake and those of low uptake and to lead to underestimation or overestimation of radiotracer concentrations. This can be the dominant source of error in quantitative SPECT studies of small structures and must be carefully considered when comparing images of different-sized objects, or sequential images of objects that are changing size (e.g., tumor shrinkage caused by therapy).

C. PERFORMANCE CHARACTERISTICS OF SPECT SYSTEMS

The following sections provide representative methods for characterizing the performance and for quality assurance of SPECT systems. A complete description of these measurements can be found in reference 11.
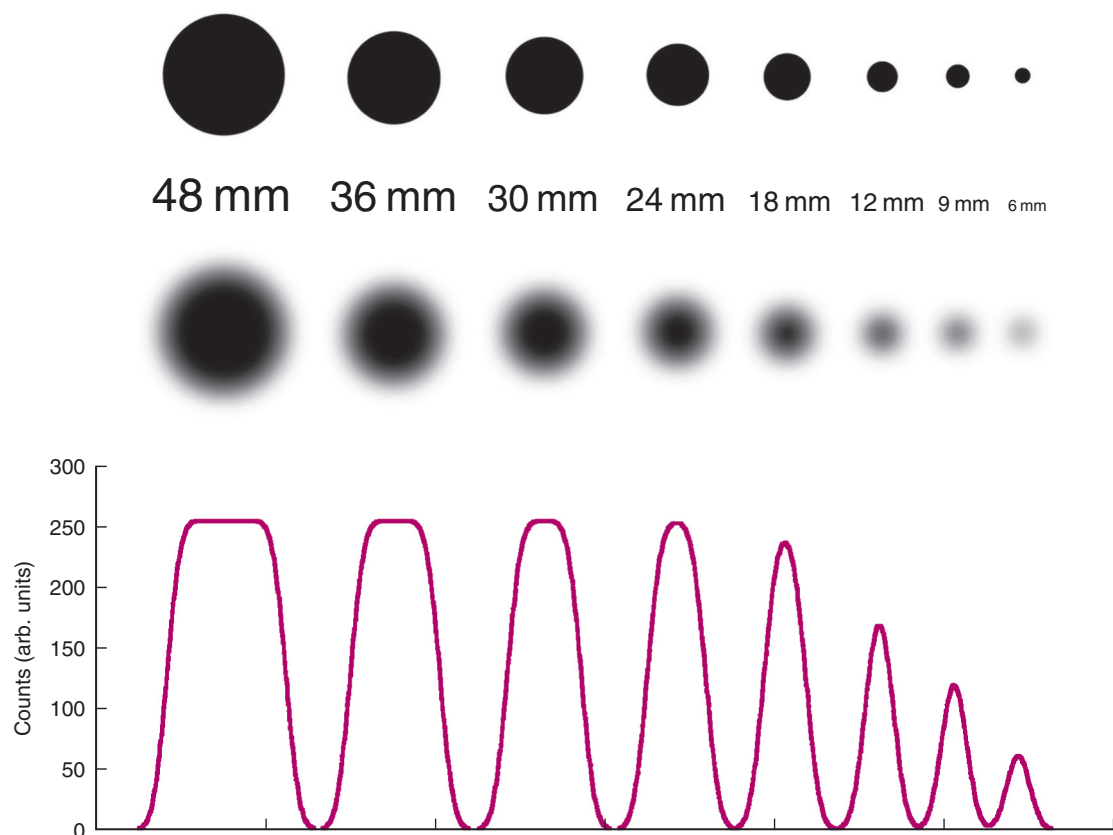
FIGURE 17-18 Illustration of partial-volume effect. The cylinders shown in the *top row* have diameters ranging from 48 mm down to 6 mm, and each contains the same concentration of radionuclide. The *middle row* shows a simulation of the images that would result from scanning these cylinders on a SPECT system with an in-plane spatial resolution of 12-mm full width at half maximum. The cylinders are assumed to have a height much greater than the axial resolution. The *bottom row* shows count profiles through the center of the images. Although each cylinder contains the same concentration of radionuclide, the intensity, and therefore the apparent concentration, appears to decrease when the cylinder size approaches and then becomes smaller than the resolution of the SPECT system. The integrated area under the count profiles does, however, accurately reflect the total amount of activity in the cylinders.
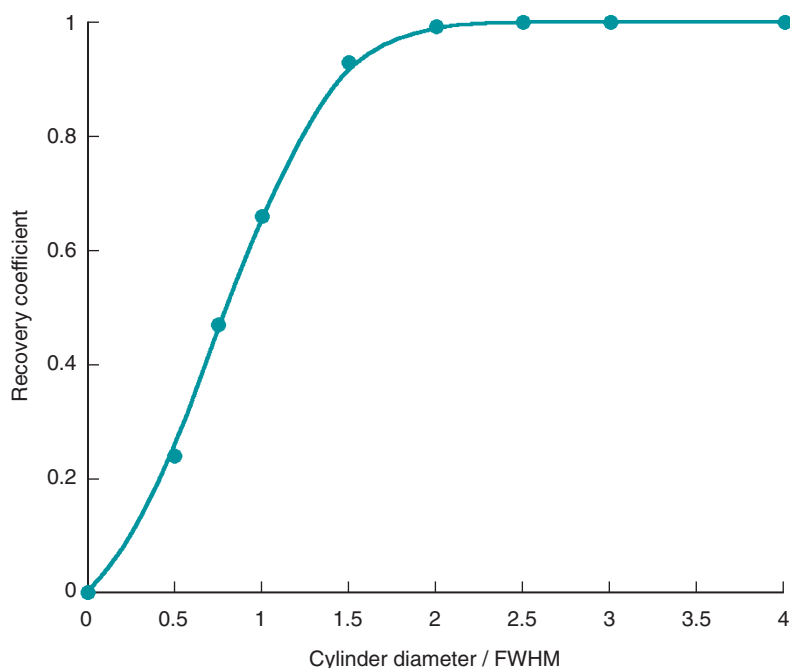

FIGURE 17-19 Recovery coefficient versus object size [in units of size/full width at half maximum (FWHM)] using the data from Figure 17-18. A recovery coefficient of 1 is obtained when the size of the object is $\gtrsim 2 \times$ FWHM. Note that the recovery coefficient depends on the radionuclide concentration in the objects of interest and in the surrounding tissue. For example, if the cylinders in Figure 17-18 contained no radionuclide and were placed in a background containing a uniform level of radionuclide, the recovery coefficients would be the reciprocal of those shown here.

1. Spatial Resolution

Spatial resolution in SPECT is characterized using profiles through the reconstructed image of a line or point source. Because the reconstructed images usually are stacked into a 3-D volume, two components of spatial resolution should be reported. *In-plane* or *transaxial resolution* refers to the component within the plane of a reconstructed slice (x- and y-direction). *Axial resolution* refers to the component that is perpendicular to the slice, along the axis of rotation of the SPECT scanner (z-direction). The latter sometimes is referred to as *slice thickness.*

In-plane resolution is determined by the intrinsic resolution of the gamma camera, the resolution of the collimator, the angular and linear sampling intervals used for acquiring the projection data, and the shape and cut-off frequency of the reconstruction filter. Of these, the dominant factor almost always is the collimator resolution (Chapter 14, Section C). Axial resolution depends on the intrinsic resolution of the gamma camera, the resolution of the collimator, and the linear-sampling interval along the axis of rotation of the gamma camera. Reconstructed spatial resolution is typically measured as follows:

A small ^{57}Co or ^{99m}Tc point source is placed in the FOV of the SPECT camera at the location of interest. To measure spatial resolution accurately, the diameter of the test source should be much smaller than the resolution capability of the imaging instrument (e.g., source diameter <1/4 of the expected FWHM resolution). Generally, measurements are made with the source at the center of the FOV and at several peripheral locations in both the axial and transaxial directions. SPECT images of the point source then are acquired using linear and angular sampling intervals normally employed in clinical practice. The image is reconstructed using a ramp filter and a pixel size that is less than 20% of the anticipated spatial resolution (FWHM). Thus, for a SPECT system with 12-mm FWHM resolution, the point-source size should be smaller than ~3 mm and the pixel size should be smaller than ~2.4 mm.

The reconstructed image of the point source is a nearly spherical dot within the 3-D image volume. A profile drawn directly through the center of the image of the point source yields the PSF. Usually, spatial resolution is characterized by the FWHM of the PSF. The FWHM is not a complete specification because PSFs of different shapes can have the same FWHM;

however, it is useful for general comparisons of imaging systems. A more complete specification is provided by the modulation transfer function, which can be obtained by taking the Fourier transform of the PSF (Chapter 15, Section B.2). PSFs and FWHMs usually are measured along the three orthogonal directions x, y, and z through the image of the point source. The average FWHM for the x- and y-axis profiles gives the transaxial resolution, whereas the FWHM of the z-axis profile gives the axial resolution.

The ramp filter provides the best achievable resolution for a specific collimator. However, as described in Chapter 16, Section B.3, it also enhances noise and often is not used clinically for this reason. If so, the measurement should be repeated for the reconstruction filters that are used in clinical practice. The measurement is repeated for different locations in the camera FOV to provide information about the uniformity of the reconstructed image resolution.

The PSF provides resolution values along three orthogonal directions. However, point sources can be difficult to manufacture, and PSFs provide values only for one image plane. Line sources and LSFs are an alternative solution for both of these limitations. If the line source is aligned parallel to the axis of the SPECT scanner, the in-plane resolution components can be measured simultaneously for all image planes. However, a second measurement with the line source rotated so that it lies perpendicular to the scanner axis then is necessary to obtain the axial resolution.

2. Volume Sensitivity

The *volume sensitivity* measurement gives the number of events detected by the SPECT system per second per unit of concentration of radionuclide uniformly distributed in a 20-cm-diameter cylinder. The result depends, among other things, on the efficiency of collimator, the energy window setting, the energy resolution of the detector, the thickness of the NaI(Tl) crystal, the radionuclide, and the number of gamma camera heads in the SPECT system.

The measurement uses a 20-cm-diameter × 20-cm-tall (outer dimensions) acrylic fillable phantom with a wall thickness between 8 and 12 mm. The phantom is filled with a known and uniform concentration A (becquerels per milliliter) of the radionuclide of interest (determined by using a dose calibrator or other calibrated radiation detector). The activity used in the cylinder is chosen such

that it leads to a gamma camera counting rate of ~10,000 cps. At this counting rate, dead time and pile-up effects are negligible.

The well-mixed phantom is placed at the center of the axis of rotation of the SPECT system. A 360-degree circular orbit SPECT scan, with a radius of rotation of 150 mm, is performed. Typically 128 projection views are acquired, with each projection view containing on the order of 100,000 counts. Uniformity corrections, or any other corrections that may alter the number of counts in the projection images, are turned off.

The total time T required to complete the acquisition and the total number of counts N recorded across all the projection views are determined. The system volume sensitivity (SVS) is then given by

$$SVS(\text{cps/Bq/mL}) = \frac{N(\text{counts})/T(\text{sec})}{A(\text{Bq/mL})}$$

(17-15)

Sometimes, the measurement is reported as the volume sensitivity per axial centimeter, in which case Equation 17-15 is divided by the axial length of the phantom, in this case 20 cm.

3. Other Measurements of Performance

Other important performance parameters of a SPECT system are energy resolution, count-rate performance, and dead time. These parameters are the same, irrespective of whether a gamma camera is used for planar imaging or for SPECT; therefore the measurements described in Chapter 14, Sections E.5 and E.6, are equally applicable to SPECT.

4. Quality Assurance in SPECT

As described in Chapter 14, Section E, quality assurance programs are important to ensure that an imaging system is functioning correctly. Many of the quality assurance procedures used for gamma cameras also serve to ensure high-quality images when the gamma camera is used for SPECT. However, there are certain differences in the requirements and additional measurements that should be made when a gamma camera is used for SPECT imaging.

One difference relates to the specifications of flood-field uniformity discussed in Chapter 14, Section E.4. In planar imaging, nonuniformities of a few percent are acceptable for producing images of diagnostic quality. In SPECT,

even smaller nonuniformities can lead to major artifacts in reconstructed images. The artifacts often appear as rings in images acquired with single-headed SPECT systems or as arcs in images acquired with multi-headed systems. The intensity of the artifact is inversely proportional to the distance of the nonuniformity from the axis of rotation. This is because nonuniformities in peripheral areas are spread across a larger area of the image during reconstruction, whereas a nonuniformity near the axis of rotation affects a concentrated area near the center of the image, which can lead to strong artifacts.

Flood-field uniformities of 1% or better are desirable for gamma camera detectors used for SPECT. To detect nonuniformities at this level, it is necessary that sufficient counts be acquired to ensure that the measurement is not limited by counting statistics. Poisson counting statistics dictate that 10,000 counts are required per image element to reach an uncertainty of 1% in a planar image (Equation 9-6). If an image matrix of 64×64 is used, a total of ~41 million counts will be required in the uniformity image.

In many cases, it also is instructive to measure the reconstructed image uniformity of a SPECT system. At the present time, there is no specific National Electrical Manufacturers Association procedure for this measurement, but a reasonable approach would be to use the data acquired using the methods described in Section C.2 for measuring volume sensitivity. An image of the uniform cylinder would be reconstructed with appropriate attenuation and scatter corrections and with the use of clinically relevant reconstruction algorithms and filters. The reconstructed images are visually inspected for any noticeable artifacts or structured noise. Care must be taken to ensure that the scatter and attenuation corrections themselves are not the cause of any artifacts.

A test that is specific to SPECT systems is the measurement of system alignment. It is critical that the mechanical center of rotation (COR) coincide with the COR defined for the projection data used for reconstruction. If the camera detector sags or wobbles as it rotates around the patient, additional blurring or ring artifacts may be introduced into the image. Because it is extremely difficult to make a mechanically or rotationally perfect gantry, most manufacturers measure the alignment of their systems prior to shipment and incorporate software that corrects on a projection-by-projection basis for any small deviations

from the COR. An additional requirement for multiheaded systems is that all the heads be accurately aligned in the axial direction. Otherwise, each head records data from a different slice, which leads to additional blurring or artifacts in the axial direction.

System alignment errors can be measured by recording profiles from different projection angles for a point source placed off-center in the FOV of the SPECT system. A typical protocol involves recording an even number of projection profiles N at equal angular intervals over 360 degrees. For example, projections could be acquired at 0, 90, 180, and 270 degrees. For each projection profile, the centroid (r_{cen}, z_{cen}) of the image of the point source on the gamma camera face is determined, in which r is the radial coordinate (as defined in Fig. 16-3) and z is the axial coordinate. The average COR error (Err_{COR}) is then given by

$$Err_{COR} = \frac{1}{N} \sum_{n=1}^{N} r_{cen} \qquad (17\text{-}16)$$

The individual x and y components of the COR error are given by averaging r_{cen} for the projection data at $\phi = 0$ degrees and 180 degrees for x and $\phi = 90$ degrees and 270 degrees for y, in which the projection angle is defined as shown in Figure 16-3. The average axial deviation Err_{AX} of the detector heads (caused by detector tilt) can be calculated from

$$Err_{AX} = \frac{1}{N} \sum_{n=1}^{N} |\bar{z} - z_{cen}| \qquad (17\text{-}17)$$

in which z_{cen} is the PSF centroid in the z direction and $\bar{z}$ is the mean value of z_{cen}. In multiheaded SPECT systems, differences in Err_{COR} and Err_{AX} between detector heads must also be assessed to determine any relative misalignment of the heads. The recommended methods for doing this can be found in reference 12.

D. APPLICATIONS OF SPECT

It is estimated that there are more than 5,000 SPECT-capable systems worldwide. Not surprisingly, the major uses of SPECT as opposed to planar imaging are for situations involving organs with complex geometry or structure, for which accurate 3-D localization of signals is critical for patient diagnosis and management.

The most frequent use of SPECT is for studies of myocardial perfusion for assessing coronary artery disease and heart muscle damage following infarction. Figure 17-20 shows a series of SPECT images that reflect perfusion of the heart. It is common to perform cardiac perfusion studies both under resting conditions and also following a "stress" to the heart created by exercise or by the injection of a drug that causes vasodilation (e.g., adenosine). These are called *rest/stress studies.*

In some cases, SPECT studies are gated to the electrocardiogram signal from the heart, and data from specific portions of the cardiac cycle (e.g., end-systolic or end-diastolic) can be isolated. This reduces blurring caused by motion of the heart and leads to improved image sharpness and contrast. However, the number of events contributing to the image are reduced (data are acquired only for a fraction of the cardiac cycle), leading to poorer signal-to-noise ratio for a fixed data
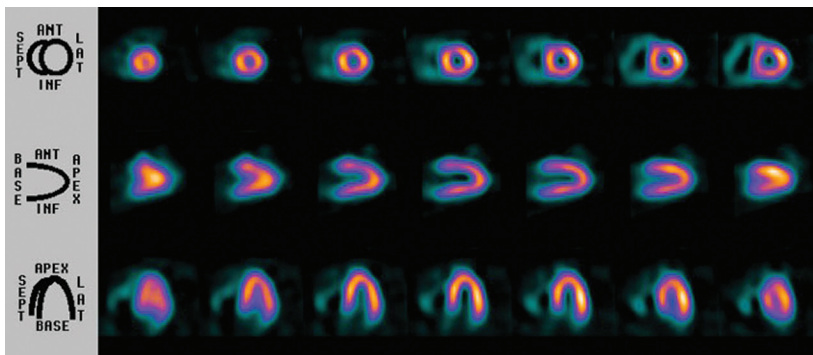

FIGURE 17-20   SPECT images showing perfusion in the heart muscle of a normal adult using ^{99m}Tc-sestamibi as the radiopharmaceutical. The image volume has been resliced into three different orientations as indicated by the schematics on the left of each image row. SPECT data were acquired over 64 views with a data acquisition time of 20 sec/view. Images were reconstructed with filtered backprojection onto a 128 × 128 image array. (*Images courtesy Siemens Medical Systems USA, Inc., Hoffman Estates, IL.*)

acquisition time. Figure 17-21 shows a comparison between gated and ungated SPECT images of the heart. Myocardial perfusion studies usually are carried out using ^{201}Tl, ^{99m}Tc-sestamibi, or ^{99m}Tc-tetrofosmin.

Cerebral perfusion studies with SPECT also are widespread, with applications including cerebrovascular disease, dementia, seizure disorders, brain tumors, and psychiatric disease (Fig. 17-22). Commonly used radiotracers are ^{99m}Tc-hexamethylpro pyleneamine oxime (^{99m}Tc-HMPAO) and ^{99m}Tc-ethyl cysteinate dimer (^{99m}Tc-ECD). A number of research groups also are developing novel SPECT radiotracers that bind to specific receptor populations in the brain, enabling the imaging of

FIGURE 17-21 Comparison of gated (*top row*) and ungated (*bottom row*) SPECT images showing perfusion in the heart muscle of a normal adult following the injection of 1100 MBq of ^{99m}Tc-sestamibi. Images were acquired on a triple-headed gamma camera with low-energy, high-resolution parallel-hole collimators. Ninety projection views were acquired in 4-degree steps (30 projections per head), and the total imaging time was approximately 20 minutes. Data acquisition started 30 minutes after radiotracer injection. Short-axis views of the heart are shown. In the gated study, the cardiac cycle is divided into eight equal time intervals. Based on the electrocardiographic trigger, events are histogrammed into the appropriate interval. The gated images in this figure correspond to the time interval that represents end-diastole. Cardiac gating leads to a small improvement in apparent image contrast by reducing blurring caused by cardiac motion. (*Images courtesy Dr. Steve Meikle, University of Sydney, Australia.*)
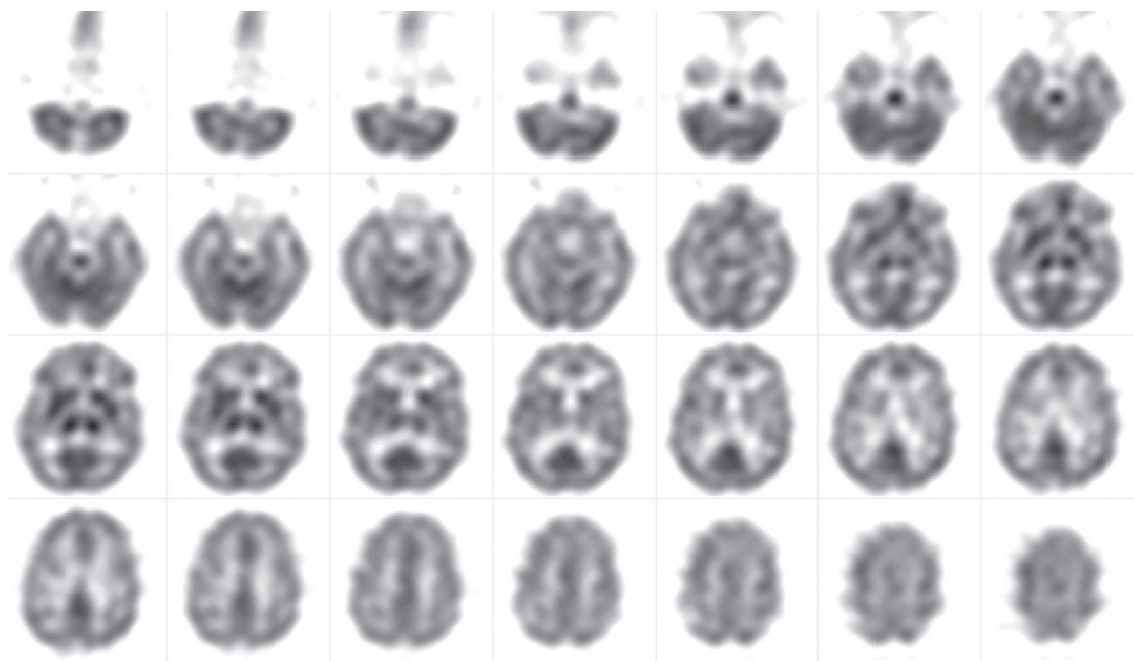

FIGURE 17-22 Transaxial SPECT images showing perfusion in the brain of a normal adult following injection of 890 MBq of ^{99m}Tc-HMPAO. Data were acquired on a triple-headed gamma camera with low-energy, high-resolution fan-beam collimators. One hundred twenty projection views were collected in 3-degree increments (40 views per camera head) with an imaging time of 40 sec/view. Total imaging time was approximately 30 minutes, with acquisition commencing 50 minutes after radiotracer injection. (*Courtesy Dr. Steve Meikle, University of Sydney, Australia.*)

important receptors such as dopamine receptors and serotonin receptors.

A third important application of SPECT is in oncology. Radiotracers such as ^{67}Ga, ^{201}Tl, and ^{99m}Tc-sestamibi often show accumulation in cancerous cells, and both primary and metastatic lesions can be visualized in SPECT images. SPECT (in comparison with planar imaging) is particularly useful for tumor imaging in the thorax, abdomen, or brain, where the tomographic information aids in tumor detection and localization against a complex background of heterogeneous tissues. New radiopharmaceuticals such as ^{99m}Tc-depreotide and ^{111}In-pentetreotide, which are specifically targeted to somatostatin receptors that are overexpressed on many malignant cells (as well as in areas of inflammation), have become available and appear promising. There also is interest in using radiolabeled
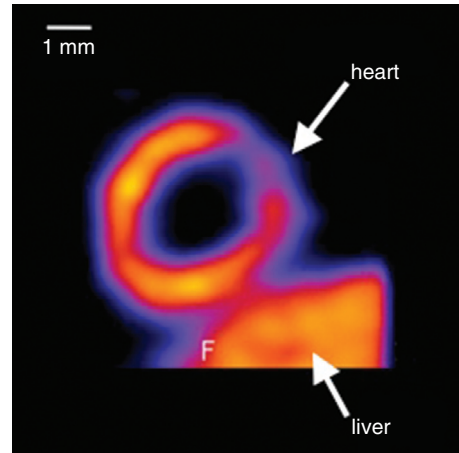

FIGURE 17-23 SPECT image showing myocardial perfusion in a mouse obtained with a small-animal system. The injected radiotracer is ^{99m}Tc-sestamibi and the study was electrocardiogram-gated. (*Courtesy Bioscan Inc., Washington D.C.*).

A. Vena cava inferior
B. Heart
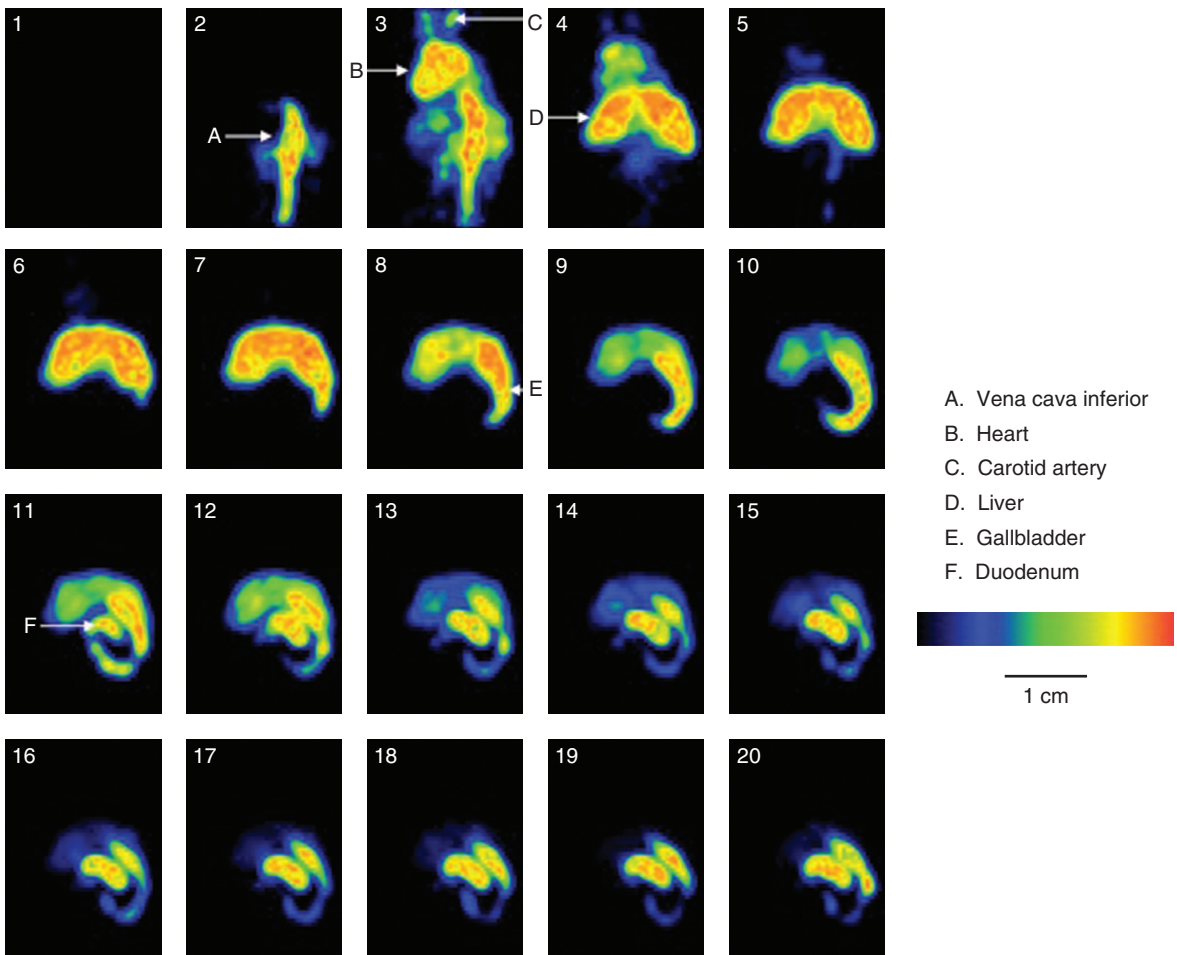C. Carotid artery
D. Liver
E. Gallbladder
F. Duodenum

1 cm

FIGURE 17-24 Dynamic SPECT images showing a single reconstructed coronal image slice over time following the intravenous injection of 34 MBq of ^{99m}Tc-HIDA into a mouse. Each image represents a 15-second acquisition over a period of 300 seconds starting at the time of injection. The dynamic sequence of images shows the temporal sequence of uptake and clearance of the radiopharmaceutical in the liver. (*Courtesy Félicie Sherer, Université Libre de Bruxelles, Belgium; Steven Staehlens, Ghent University, Belgium; and Freek Beekman, Delft University of Technology, The Netherlands*).

antibodies and peptides for tumor localization, and ultimately also for tumor therapy by substituting the imaging radionuclide with a β emitter that can cause localized cell death.

Other areas in which SPECT is used include imaging of infection and inflammation and measurement of liver and kidney function. An extensive discussion of the clinical applications of both planar gamma camera imaging and SPECT can be found in reference 13.

SPECT also has seen growing use for preclinical studies and basic biomedical research, often with dedicated small-animal SPECT systems such as those described in Section A.4. Studies may be performed in small animals to study the biodistribution over time of a potential new therapeutic entity, for example peptides, antibodies, nanoparticles, or cells that have been radiolabeled to allow them to be imaged. A second common use is to measure the effect of a new therapy. For example, the ability of implanted stem cells to improve myocardial perfusion could be monitored by SPECT in an animal model using the same radiotracers for perfusion that are used in the clinic. Figure 17-23 shows perfusion images of the myocardium in a mouse obtained with a small-animal SPECT system. Figure 17-24 shows a single image slice from a fast dynamic SPECT study showing the uptake of the radiopharmaceutical ^{99m}Tc-HIDA (see Table 5-5) in the liver following injection into a mouse. Some of the major applications for small-animal SPECT systems are discussed in reference 14.

REFERENCES

1. Rogers WL, et al: SPRINT II: A second-generation single-photon ring tomograph. *IEEE Trans Med Imag* 7:291-297, 1988.
2. Genna SG, Smith AP: The development of ASPECT, an annular single-crystal brain camera for high-efficiency SPECT. *IEEE Trans Nucl Sci* 35:654-658, 1988.
3. Babla H, Bai C, Conwell R: A triple-head solid state camera for cardiac single photon emission tomography (SPECT). *Proc SPIE* 6319:63190M, 2006. DOI: 10.1117/12.683765.
4. Erlandsson K, Kacperski K, van Gramberg D, Hutton BF: Performance evaluation of D-SPECT: a novel SPECT system for nuclear cardiology. *Phys Med Biol* 54:2635-2649, 2009.
5. CardiArc. Accessed October 11, 2011 from http://www.cardiarc.com.
6. Meikle SR, Kench P, Kassiou M, Banati RB: Small-animal SPECT and its place in the matrix of molecular imaging technologies. *Phys Med Biol* 50:R45-61, 2005.
7. Sorenson JA: Quantitative measurement of radioactivity in vivo by whole-body counting. In Hine GJ, Sorenson JA, editors: *Instrumentation of Nuclear Medicine*, Vol 2, New York, 1974, Academic Press, pp 311-348.
8. Chang LT: A method for attenuation correction in radionuclide computed tomography. *IEEE Trans Nucl Sci* 25:638-643, 1978.
9. Jaszczak RJ, Chang LT, Stein NA, Moore FE: Whole-body single-photon emission computed tomography using dual, large-field-of-view scintillation cameras. *Phys Med Biol* 24:1123-1142, 1979.
10. Bailey DL: Transmission scanning in emission tomography. *Eur J Nucl Med* 25:774-787, 1998.
11. King MA, et al: Attenuation, scatter and spatial resolution compensation in SPECT. In Wernick MN, Aarsvold JN, editors: *Emission Tomography: The Fundamentals of PET and SPECT*, Amsterdam, 2004, Elsevier Academic Press, pp 473-498.
12. Performance Measurements of Scintillation Cameras: *National Electrical Manufacturers Association (NEMA) Standards Publication NU 1-2007*. Rosslyn, VA, 2007, NEMA.
13. Sandler MP, et al, editors: *Diagnostic Nuclear Medicine*, ed 4, Baltimore, 2002, Lippincott Williams & Wilkins.
14. Franc BL, Acton PD, Mari C, Hasegawa BH: Small-animal SPECT and SPECT/CT: Important tools for preclinical investigation. *J Nucl Med* 49:1651-1663, 2008.